5

Passive radiative cooling of silicon solar modules with silica microcylinder arrays

Passive radiative cooling (PRC) is a method to dissipate excess heat from a material into or through the earth's atmosphere by the spontaneous emission of infrared (IR) thermal radiation. Photovoltaic systems can benefit from PRC by lowering the system's operating temperature. In particular, for a (silicon) solar cell, the challenge is to enhance PRC while simultaneously retaining transparency for sunlight above the (silicon) bandgap. Here, we propose a hexagonal array of cylinders etched into the top surface of the solar cell module glass to enhance PRC. We use FDTD simulations to optimize the cylinder geometry to enhance the emissivity in the IR spectral range. Multipolar Mie-like resonances in the cylinders are shown to cause anti-reflection effects in the IR, which results in enhanced IR emissivity. Next, the optimized structures are fabricated by UV-lithography and reactive ion etching. Using integrating sphere Fourier transform infrared (FTIR) spectroscopy, we measure the emissivity of the silica cylinder array, and find good correspondence to the simulated results. The fabricated microstructure increases the average emissivity between λ = 7.5 - 16 μm from 84.3% to 97.7%, without reducing visible light transmission. Our design procedure offers a PRC structure for any photovoltaic device, with or without module glass encapsulation, and any other outdoor device that benefits from a lower operating temperature.

5

This chapter is based on:

Passive radiative cooling of silicon solar modules with silica microcylinder arrays
Evelijn Akerboom*[1], Tom Veeken*[1], Chris Hecker[2], Jorik van de Groep[3], and Albert Polman[1]
in preparation
*Evelijn and Tom contributed equally to this work.

[1]Center for Nanophotonics, NWO-Institute AMOLF, Science Park 104, 1098 XG Amsterdam, The Netherlands
[2]Department of Earth Systems Analysis, Faculty of Geo-Information Science and Earth Observation (ITC), University of Twente, Hengelosestraat 99, 7500 AA Enschede, The Netherlands
[3]Van der Waals-Zeeman Institute, Institute of Physics, University of Amsterdam, Science Park 904, 1098 XH Amsterdam, the Netherlands

Author contributions:
Tom and Albert conceived the project. Evelijn fabricated the microcylinder arrays, and performed the transfer matrix model calculations and the data analysis. Evelijn and Tom performed the FDTD simulations and visible-NIR hemispherical reflection measurements. Evelijn and Chris performed the infrared hemispherical reflection measurements. Tom wrote the original draft. Albert supervised the project. Jorik and Albert reviewed and edited the manuscript. All authors provided feedback and contributed to the manuscript.

5.1 Introduction

Over the past few decades, significant effort has been put into improving the power conversion efficiency of solar cells [15]. The detailed balance limit [12] calculates a fundamental efficiency limit of 29.7% for silicon-based solar cells [169], not far from the current record efficiency of 27.6% [170]. Solar cell efficiency measurements are performed at standardized testing conditions, e.g., 1 sun illumination at an operating temperature of 25 °C. However, due to hot-carrier cooling and non-radiative recombination, a silicon solar cell typically reaches operating temperatures of 60 °C under direct sunlight, and even as high as 80 °C [171]. Elevated operating temperatures reduce the power conversion efficiency and the operating lifetime of the cell. This efficiency reduction is mainly attributed to a decrease in the open-circuit voltage due to increased recombination rates [172]. An average relative efficiency drop of -0.45% has been shown for every 1 °C temperature rise of mono- and poly-crystalline silicon solar modules [173]. A temperature increase from 25 to 60 °C amounts to a significant -15.75% efficiency drop. Even though the effects of elevated operating temperatures on the operating lifetime of a silicon solar module have not been isolated [174], it is expected to negatively impact all degradation modes [175, 176]. These adverse temperature effects emphasize the need for a method to cool Si solar modules. Here, we investigate the enhancement of passive radiative cooling (PRC) to decrease the operating temperature of a Si solar cell. The concept of PRC leverages the thermal emission of an object to dissipate heat to lower its temperature. According to thermodynamics, two objects with different temperatures will exchange heat via thermal radiation until an equilibrium temperature is reached. The Stefan-Boltzmann law states that the amount of heat emitted as thermal radiation scales with the temperature of an object as $\propto T^4$, so effectively, heat is transferred from the warmer object to the colder object. Thus, to cool a hot object with thermal emission, a colder object is needed to function as the heat sink. Outer space is the perfect heat sink due to the temperature of about 3 K and the immense volume, which makes it a heat sink with practically infinite capacity. The concept of emitting thermal radiation into outer space is the core principle of PRC.

During the last two decades, interest in PRC has grown for several applications [177], from dew collection in remote and dry places [178] to the cooling of buildings [179]. In 2014, Raman et al. showed a 4.9 °C sub-ambient daytime cooling using a thin-film multilayer to optimize the radiative properties of the structure [180]. The multilayer was designed to enhance PRC while simultaneously excluding heating by reflecting incident solar radiation. However, the high reflectance of this geometry in the visible spectral range makes it particularly unsuitable for solar cells applications. A solar cell absorbs light with photon energy larger than the bandgap energy, including visible wavelengths.

Over the past years, several different materials and methods have been explored to cool solar cells with PRC: multilayers [181, 182], 2D structures [183–188], a combination of a multilayer and 2D structures [189, 190], or an effective medium approach [191–193]. Table 5.1 lists the calculated (italic) or fabricated (bold) material systems of a few notable works, and their reported temperature reduction: calculated values are in italic, measured values in bold font. To enable comparison of the achieved temperature reductions, it is important to specify the reference material system. This is particularly important since bare silicon exhibits practically no PRC while a standard glass cover achieves significant PRC. Jaramillo-Fernandez et al. demonstrated the largest temperature reduction, both with respect to a bare silicon substrate and silicon covered with silica glass [184]. They placed a self-assembled monolayer of silica spheres on top of the silicon and silicon-silica reference samples and measured an average temperature reduction of 14 and 9 °C, respectively. Although the layer of spheres performs well, it may suffer from structural degradation in outdoor conditions.

Here, we propose resonant microstructures to enhance the PRC of a silicon solar module by etching them into the module glass. The design enhances the cooling power while keeping the structure transparent in the visible and near-infrared wavelength range. First, we theoretically derive a general condition for the ideal optical properties to achieve maximum PRC in a silicon solar module. Then, we use numerical finite-difference time-domain (FDTD) simulations to design a microcylinder array on top of a quartz silica module glass to enhance PRC compared to the flat silica reference. We fabricate the optimized design by UV photolithography and reactive ion etching. Hemispherical reflection measurements in the IR are performed to obtain the experimental emissivity spectra, which correspond very well to the simulated results. The average emissivity between λ = 7.5 - 16 µm is increased from 84.3% (silica reference) to 97.7%, which results in a calculated reduction of 3 K in the equilibrium temperature. Finally, we show that the silica substrate with a microcylinder array remains transparent in the visible and near-infrared (NIR) wavelength ranges.

Table 5.1: *Advances of passive radiative cooling for solar cells. The PRC structure, the reference sample, and the calculated (italic) or measured (bold) temperature reduction are listed.*

First Author (year) [reference]	**Passive radiative cooling structure**	**Reference sample**	**Temperature reduction (K)**
Zahir (2021) [182]	Multilayer: *TiO_2/BK7*	Si solar cell Si + SiO_2	*18.4* *5.4*
Perrakis (2021) [183]	2D structure: *SiO_2 square micro grating with nanopillars on top*	Si Si + SiO_2	*5.8* *0.2*
Jaramillo-Fernandez (2019) [184]	2D structure: **self-assembly of SiO_2 spheres**	Si Si + SiO_2	**14** **9**
Long (2019) [185]	2D structure: **SiO_2 square lattice of micro-cylinders**	Si Si + SiO_2	*20* **2**
Zhu (2015) [188]	2D structure: **lattice of air holes in SiO_2**	Si Si + SiO_2	**13** **1**
Zhao (2018) [190]	Multilayer+2D structure: *TiO_2/SiO_2 with a lattice of air cylinders*	Si solar cell Si + SiO_2	*12* *8.3*
Chen (2021) [192]	Effective medium: **polymer matrix with embedded SiO_2 nanoparticles**	Si solar cell	**5**
Akerboom (2022) [this work]	2D structure: **SiO_2 microcylinder array**	Si Si + SiO_2	*21* *3*

5.2 Passive radiative cooling

The concept of passive radiative cooling (PRC) is based on the thermal balance of a solar cell. In Figure 5.1a, a schematic representation of the energy balance of a solar cell is shown, indicating the four main power terms that determine the equilibrium temperature of the cell: the absorbed radiation coming from the sun (P_{sun}), the absorbed thermal radiation from the atmosphere (P_{atm}), the thermal radiation the solar cell is emitting (P_{rad}), and the power lost or gained by convection (P_{conv}). Here we assume that heat conduction via connection to the rooftop is negligible. The total cooling power is given by the sum of the four main powers,

$$P_{cool} = P_{rad} + P_{sun} + P_{atm} + P_{conv}. \tag{5.1}$$

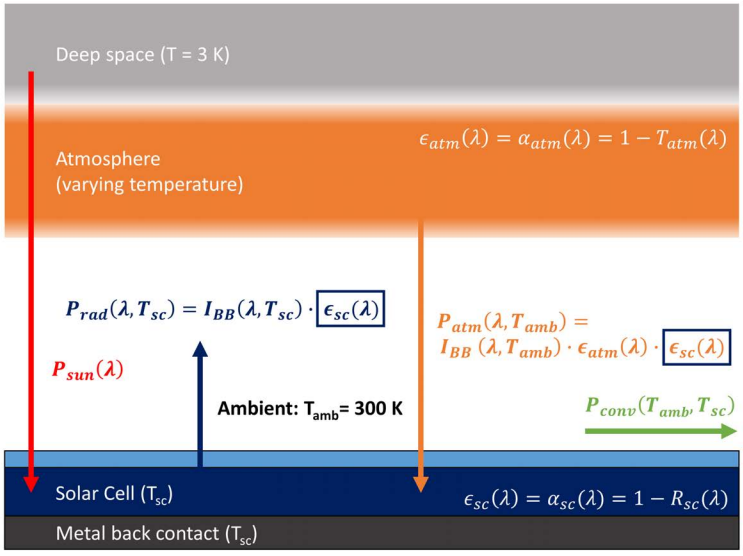

Figure 5.1: *Schematic representation of the incoming and outgoing power flows that govern the equilibrium temperature of a solar cell (T_{sc}). The solar cell reaches its equilibrium temperature when the power from the sun (P_{sun}) and the thermal radiation from the atmosphere (P_{atm}) are in balance with the thermal radiation emitted by the solar cell (P_{rad}) and the power flow by convection and conduction (P_{conv}).*

When the total cooling power is zero, there is no net heat flux, and the solar cell has reached equilibrium temperature. A positive cooling power will effectively reduce the temperature, while a negative cooling power indicates the solar cell is heating up. Figure 5.1 shows a schematic representation of the power flows in Eq. (5.1) — a detailed analysis of the interplay is provided in the Methods section. For a constant incident solar power (P_{sun}) (Fig. 5.2a) and (P_{conv}), we find that the cooling power depends on:

$$P_{cool}(T_{sc}, T_{amb}) \propto \int \left(I_{BB}(\lambda, T_{sc}) - I_{BB}(\lambda, T_{amb})\epsilon_{atm}(\lambda)\right)\epsilon_{sc}(\lambda)d\lambda. \tag{5.2}$$

Here, T_{sc} and T_{amb} are the temperatures of the solar cell and ambient, respectively, I_{BB} is the intensity of the blackbody spectrum, ϵ_{atm} is the emissivity of the atmosphere, and ϵ_{sc} the emissivity of the solar cell.

Figure 5.2b shows the ideal blackbody spectra at ambient temperature (300 K) and a typical solar cell operating temperature (340 K). The spectrum of a non-ideal blackbody is obtained by multiplying the ideal spectrum by the emissivity. By photonic engineering of the emissivity, we can explore the effect of an emissivity spectrum on the resulting equilibrium temperature. First, we consider the upper temperature bound of zero emissivity for energies above the solar cell bandgap, plotted in Fig. 5.2c in red. Calculating the cooling power with Eq. (5.1), we obtain the red curve in Fig. 5.2d and an equilibrium temperature of 366.5 K. Second, we consider an emissivity window that is unity only in the main atmospheric transmission window between 8 - 14 µm, as shown in Fig. 5.2c in green. This is the ideal emissivity spectrum for a solar reflector, enabling it to cool below ambient temperature by radiating through the atmosphere while keeping heat from the sun and atmosphere out. However, when used for a solar absorber material like a silicon solar cell, the resulting PRC is sub-optimal with an equilibrium temperature of 341.5 K, as shown in Fig. 5.2d in green. Third, we consider a solar absorber at a temperature higher than ambient. Due to this higher temperature, it emits more blackbody radiation than it receives from the atmosphere — see the intensity difference plotted in Fig. 5.2b. Therefore, a solar absorber can achieve higher PRC by setting its emissivity to 1 throughout its entire blackbody radiation spectrum, from 3 - 30 µm, as plotted in blue in Fig. 5.2c. Below 3 µm, the blackbody radiation at 340 K is negligible; thus, we set the emissivity to 0 between the silicon bandgap and 3 µm. This emissivity spectrum achieves the minimum equilibrium temperature at 330.5 K. We color the background of Fig. 5.2d purple to indicate the attainable equilibrium temperatures to be used as a reference for the final results. In the next section, we look at the PRC of a silicon solar cell stack and improve the PRC with a photonic cylinder array.

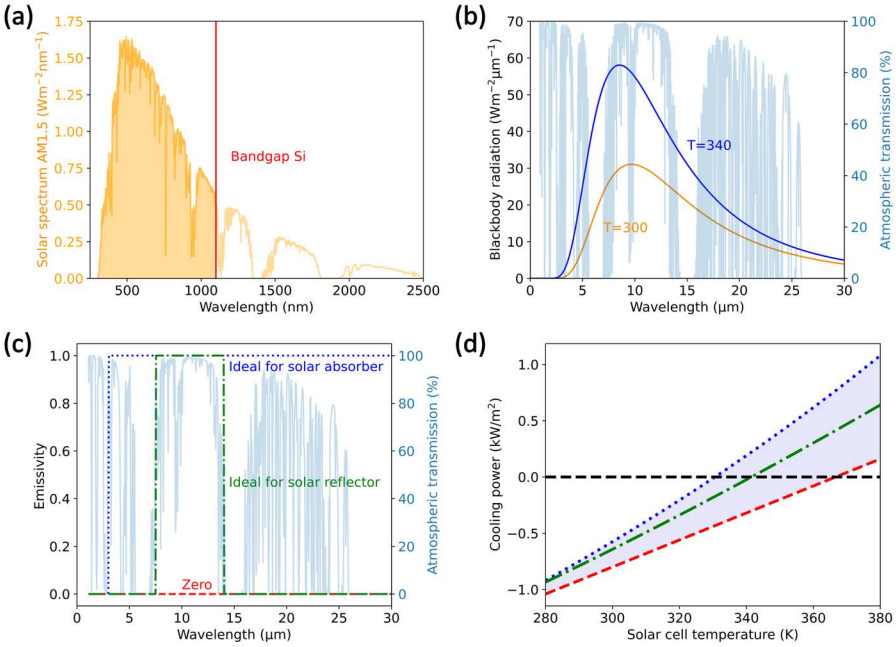

Figure 5.2: *(a) AM1.5G solar irradiation spectrum (yellow line) as a function of wavelength, the bandgap of silicon (red line), and the part of the solar spectrum that can be absorbed by silicon (yellow surface). (b) Blackbody radiation spectra for an object at 300 K (orange) and 340 K (blue), and the atmospheric transmission (light blue). (c) Step function of three emissivity spectra: zero emissivity (red), a non-zero emissivity only in the main atmospheric transmission window (green), and the ideal emissivity for a body at 340 K (blue). (d) The calculated cooling power versus solar cell temperature (Eq. (5.1)), corresponding to the emissivity spectra in (c). The equilibrium temperature is reached when the cooling power is zero.*

5.3 Photonic design

In the previous section, we have derived a condition for the ideal emissivity of a solar cell: unity emissivity for wavelengths larger than 3 µm. The silicon solar cell itself has zero absorptivity (extinction coefficient) throughout the IR wavelength range (see Fig. 5.6 in the Methods section), and thus zero emissivity (the reciprocity between absorptivity and emissivity according to Kirchoff's law is described in the Methods section). Therefore, we need to add a material to the solar cell to improve its PRC capacity, which is in thermal equilibrium with the solar cell. A typical solar module has a glass cover on top of the silicon, making it an obvious choice. Figure 5.6 also shows the absorptivity of quartz silica (SiO_2), borosilicate glass, and soda-lime glass (SLG). Beyond 7.5 µm, their extinction coefficient is non-zero, making them much more suitable materials for PRC than silicon.

We use a transfer matrix model (TMM, see Methods for details) to calculate the reflectivity of a solar module geometry consisting of a silicon substrate with a gold coating on the backside (solar cell back contact) and a quartz silica substrate on the top. The gold coating eliminates any transmission of light through this stack, and thus we can compute the emissivity as 1-R_{sc}, as shown in Fig. 5.3a in red. The emissivity of the silica-on-silicon stack is much higher than the reference without silica, which is only slightly above zero due to parasitic absorption in the Au back coating (Fig. 5.3a in green). The dip in the emissivity spectrum of the silica-on-silicon stack at 9 µm wavelength is caused by enhanced reflection at the air-silica interface. The enhanced reflection is a direct consequence of the strong fluctuation of the complex optical constants of silica in this spectral range, which is attributed to the asymmetric stretching vibration of Si-O-Si bridges [194]. Even though we defined the ideal emissivity as unity until λ = 30 µm in the previous section, we carried out simulations until λ = 16 µm because this was the range of the experimental emissivity data.

In Table 5.1, we have already seen that significant calculated and measured temperature reductions have been achieved with 2D structures for enhanced PRC. However, only Zhu et al. made use of the solar cell module glass for their experimental PRC results, which would be ideal for practical reasons. They enhanced PRC by etching deep hollow cylinders, improving anti-reflection due to the gradual refractive index change [188]. While this does enhance PRC, this approach does not include optimization for specific wavelengths. Therefore, we propose direct integration of a thinner 2D microstructure in the module glass, which we can optimize thoroughly. The microstructures should minimize the reflection between 7.5 and 16 µm wavelength (to minimize the dip in the red curve in Fig. 5.3a) and simultaneously retain transparency for sunlight with photon energies above the silicon bandgap. To achieve anti-reflection, we design a hexagonal array of silica microcylinders on the silica substrate. These structures exhibit Mie-like resonances when their size is on the order of the wavelength [164]. These types of resonant structures have received much attention in the field of nanophotonics [195, 196]. For photovoltaics, in particular, Mie-like resonant structures have been used to enhance light trapping [197], design solar cells with structural colors [36], and achieve anti-reflection for incident sunlight [24, 26]. Here, we design cylinders of several micrometers in size to achieve resonant anti-reflection for IR instead light. We use finite-difference time-domain (FDTD) simulations to optimize the dimensions of the hexagonal cylinder array (see Methods for technical details). We varied the cylinder diameter, height, and array pitch to minimize the reflection in the 4 - 16 µm wavelength range, finding the optimum for a diameter of 3.5 µm, a height of 2.25 µm, and a 6.125 µm pitch in a hexagonal array. The calculated emissivity is plotted in Fig. 5.3a in blue, showing a significant increase compared to flat silica.

To gain an understanding of the resonant anti-reflection effect of the microcylinder array, we analyze the modal scattering contribution to the reflection spectrum. We attribute

the anti-reflection effect to forward scattering of incident light by the multipolar Mie-like modes in the cylinders. According to the (generalized) Kerker condition, forward scattering is typically achieved by the interference of at least two different Mie-like modes according to the (generalized) Kerker condition [198, 199]. Figure 5.3b shows the contributions of several Mie-like modes to the extinction cross-section of a single microcylinder, decomposed using the method outlined by Evlyukhin et al. [71]. The decomposition shows that the main broad contribution comes from the electric and toroidal dipoles (ED+TD). The magnetic dipole (MD) and electric quadrupole (EQ) contributions are slightly detuned from each other. When we consider the coherent excitation of these multipolar modes by a normal-incident plane wave, the modes oscillate in phase with each other. The symmetry of the modes leads to constructive interference between the ED and MD/EQ in the forward direction (transmission) and destructive interference in the backward direction (reflection). A 'pure' Kerker condition of zero backscattering is achieved when the amplitude between the ED and MD/EQ are equal — this condition is typically only met for distinct wavelengths. Here, we achieve enhanced forward scattering by imperfect destructive interference of the ED and MD+EQ over a broad wavelength range. Further improving the destructive interference due to a better balance of the mode's amplitudes might be possible by changing the shape of the resonator. However, deviating from a radially symmetric shape also yields a polarization-dependent response. Moreover, destructive interference due to the interaction of multiple resonators or lattice modes is challenging with thermal sources [200], as we discuss next.

In general, interference between modes such as the Mie-like modes discussed above relies on a coherent phase-relation between them. However, the thermal emission that we consider as the source has only limited spatial coherence, typically on the order of $\lambda/2$ [201]. Between 8 - 16 µm wavelength, the coherence length would be 4 - 8 µm, which is larger than the size of the designed cylinder. That suggests that single-particle resonances such as the Mie-like modes, and their interference within the same particle, can be excited by thermal emission.

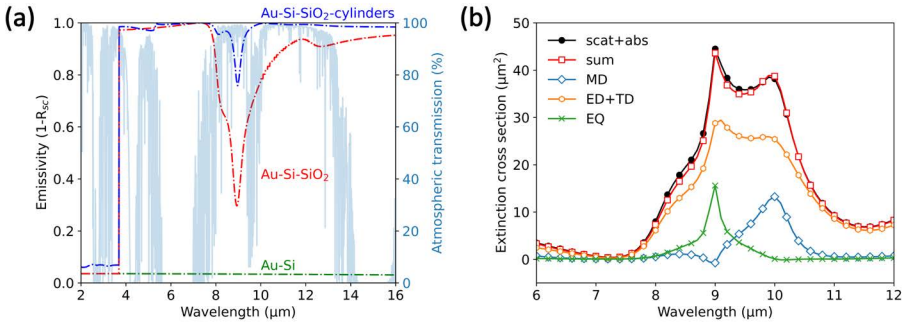

Figure 5.3: *(a) Calculated emissivity of a stack of double-side polished silicon coated with gold (Au-Si), with a silica layer on top (red) and a silica layer (blue) with the optimized geometry of silica cylinders (radius of 1.75 µm, height of 2.25 µm and a pitch of 6.125 µm). Atmospheric transmittance is shown in light blue. The patterned module glass reduces and narrows the emissivity dip of glass at 9 µm, improving the radiative cooling of the stack. (b) Multipole decomposition for a silica cylinder (radius 1.75 µm, height 2.25 µm), where the contribution of several resonances to the total extinction cross-section is shown. The silica cylinder exhibits a broadband electric- (ED) and toroidal dipole (TD), in combination with a narrower magnetic dipole (MD) and electric quadrupole (EQ).*

5.4 Fabrication

Based on the theory and simulations of the previous section, we fabricate the hexagonal microcylinder array on top of a silica substrate. A double-side polished (DSP) silicon wafer with a gold coating on the back (see Methods) is placed under the silica to replicate a simple solar absorber (see Fig. 5.4a). We used UV photolithography and subsequent reactive ion etching to realize the microcylinder array on top of a silica substrate (see Methods for details). An optical micrograph of the finalized array covering a 24 × 24 mm^2 silica substrate is shown in Fig. 5.4b, showing a uniform cylinder array and homogeneous color. Figure 5.4c shows a scanning electron microscope (SEM) image of a crosscut of the microcylinders, from which we determine a diameter of 3.65 µm and height of 2.20 µm, almost identical to the target dimensions of 3.50 (+4%) and 2.25 µm (-2.5%), respectively. The pitch is precisely 6.125 µm as designed. High transparency of the sample for visible light is visually demonstrated in Fig. 5.4d, which shows a photograph of the sample on top of the AMOLF logo.

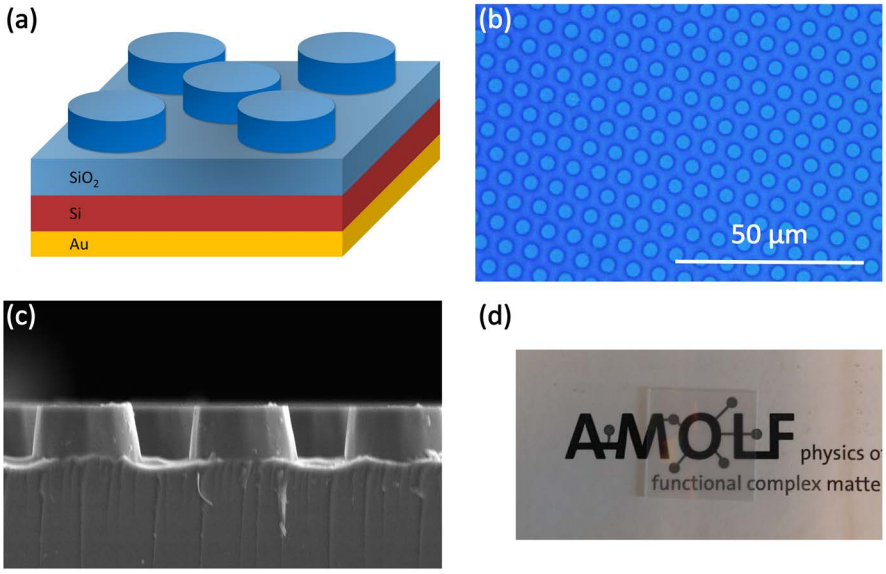

Figure 5.4: *(a) Schematic representation of the hexagonal silica microcylinder array on top of a solar module stack. (b) Optical microscopy image of the array. (c) An SEM image of a crosscut of the fabricated microcylinders, revealing straight and slightly slanted sidewalls. (d) Photograph of the microcylinder array sample (24 × 24 mm^2) on top of the AMOLF logo, showing high transparency in the visible spectral range.*

5.5 Hemispherical reflection measurements

To characterize the IR emissivity of the fabricated microcylinder array sample, we measure the hemispherical reflectance in a Fourier-transform infrared (FTIR) spectrometer (see Methods). Figure 5.5a shows the calculated emissivity spectra (dashed, shown before in Fig. 5.3a) and the experimentally obtained spectra (solid). The reference case of a bare double-side polished silicon substrate with a gold coating on the back is plotted in green. The calculated spectrum is almost zero (~3.5%) because the extinction coefficient of Si is zero beyond λ = 1150 nm. However, the measured emissivity is significantly higher beyond λ = 9 µm, which we attribute to intraband transitions in the slight n-type doped silicon substrate [202]. This small discrepancy does not influence our subsequent results because any IR light transmitted into the silica substrate is already absorbed before reaching the silicon substrate underneath. Thus, we can model the silicon to be non-absorptive in the IR.

The measured emissivity of a flat silica substrate on top of a silicon substrate is shown in Fig. 5.5a in red. An air gap between the silica and silicon substrates was avoided by adding a layer of immersion oil in between for the optical measurements. Beyond λ = 5 µm, the experimental emissivity is almost identical to the calculated spectrum. This result validates the experimental setup and the optical constants of silica that were used in the calculation. Moreover, this also validates that the thermal light source has the required coherence to excite the designed resonant modes: while we do not measure blackbody radiation, the excitation source is a thermal Globar source. The discrepancy between the calculated and experimental spectra in the range of 2 - 5 µm is attributed to a slight mismatch between the optical constants used for the calculation and the actual optical constants of the silica substrate. The absorption onset is quite abrupt for the literature values, just below 4 µm, while the actual values seem to gradually increase between 2 - 5 µm and exhibit more spectral features.

The measured emissivity of the silica substrate with the microcylinder array on top also resembles very well the calculated spectrum, as shown in Fig. 5.5a in blue. Over a broad range from 7.5 to 16 µm, a significant increase in the emissivity was found, precisely as designed. The dip in the emissivity spectrum at 9 µm wavelength is reduced from 30% to 70%. Moreover, the average emissivity between 7.5 and 16 µm is increased from 84.3% to 97.7%.

Based on the experimental emissivity spectra, we now calculate the total cooling power as a function of operating temperature. Figure 5.5b shows three cooling power curves corresponding to the measurements in Fig. 5.5a. The purple-colored background indicates the theoretical area between the upper and lower temperature bounds, as calculated in Fig. 5.2d. At zero cooling power, we find the equilibrium temperature. As expected, we find that the silicon substrate with only the gold coating performs very poorly with an equilibrium temperature of 360 K, close to the maximum of 366.5 K. The addition of the flat silica substrate moves the curve closer to the minimum equilibrium temperature. The optimized silica microcylinder substrate pushes the equilibrium temperature even further towards the theoretical minimum. The flat silica stack and microcylinder silica stack reach equilibrium temperatures of 339 and 336 K, respectively, close to the minimum of 330.5 K. Interestingly, the flat silica substrate already achieves high PRC performance due to its near-ideal optical constants, realizing a cooling potential of 21 K compared to the bare silicon reference. The microcylinders decrease the equilibrium temperature by another 3 K. Assuming a 0.45% increase in efficiency per degree cooling, this temperature reduction would result in a relative efficiency increase of 1.35 – 10.8%, depending on the PRC capability of the reference module cover. These values overestimate the equilibrium temperatures because they are based on experimental emissivity data up to λ = 16 µm (Fig. 5.5a). In contrast, the theoretical maximum is based on unity emissivity until λ = 30 µm (Fig. 5.2c).

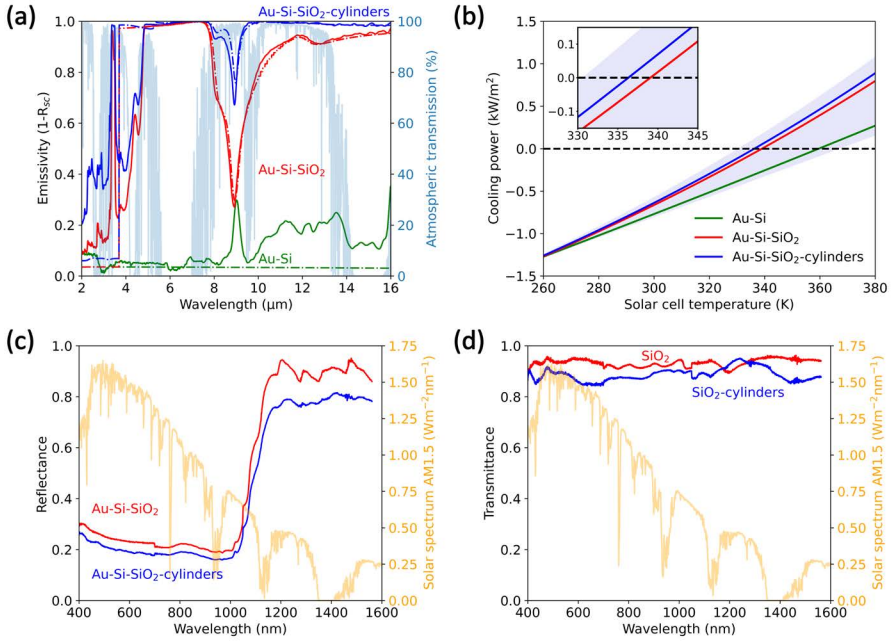

Figure 5.5: *(a) Measured (solid) and calculated (dashed) IR emissivity of silicon without module glass (green), with flat silica module glass (red), and with microcylinder module glass (blue). The microcylinder array significantly increases the emissivity in the main atmospheric transmission window (light blue, 7.5 - 14 μm). (b) Calculated cooling power versus solar cell operating temperature corresponding to the measured emissivity in (a). The purple-colored background indicates the theoretical bounds as calculated in Fig. 3b. The inset shows a zoom-in of the calculated equilibrium temperatures (zero cooling power) for comparison with the theoretical minimum equilibrium temperature. (c) Measured visible to near-infrared hemispherical reflectance of silicon with flat silica module glass (red) and microcylinder module glass (blue). (d) Measured visible to near-infrared hemispherical transmittance of the flat silica module glass (red) and microcylinder module glass (blue). The results in (c,d) show that the silica substrate remains transparent for wavelengths smaller than the silicon bandgap after adding the microcylinder array on top and even slightly improves absorption in the silicon substrate due to light trapping.*

The calculated equilibrium temperature corresponds well with the range of values listed in Table 5.1. An exact comparison of the reported temperature reductions is not possible because the calculation methods are not identical: the exact wavelength span and the optical constants vary. However, the results do show that choosing a proper module cover impacts the equilibrium temperature significantly. This is important for flat pane (silicon) solar cells, as discussed here, and concerns the development of flexible thin-film solar cells that use thin plastic module covers.

Finally, we perform hemispherical reflectance and transmittance measurements in the visible to near-infrared (NIR) spectral range to verify that the fabricated microcylinder arrays do not adversely affect the transmission of sunlight into the solar cell for energies above

the Si bandgap. Figure 5.5c shows the experimental reflectance for the two silicon-silica stacks. The reflectance is around 20% up to the silicon bandgap, mostly due to reflection at the silica-silicon interface. Beyond 1100 nm, the reflectance is higher because the gold coating at the back reflects most NIR light. This is significantly higher than the reflection of commercial solar modules, which achieve only a few percent reflection due to anti-reflection coatings and/or textures. The comparison in Fig. 5.5c shows that the microcylinders slightly decrease the reflection of light for wavelengths smaller than the silicon bandgap. We attribute this to the trapping of light that is scattered by the array into the Si. Figure 5.5d shows the experimental transmittance for the same two silica substrates without the silicon substrate. The flat silica substrate shows transmission of about 90%, typical of transmission through two silica-air interfaces. The microcylinder array shows slightly lower transmittance than the flat silica substrate over almost the entire wavelength range. This difference is again explained by light trapping: light is scattered by the microcylinders and trapped in the silica substrate by total internal reflection, reducing the transmission. When the silicon substrate is placed in contact, this scattered light does not undergo total internal reflection but instead transmits into the silicon, adding to the absorption and thus a lower reflection, as seen in Fig. 5.5c.

5.6 Conclusions

This work shows that the passive radiative cooling (PRC) power of a silicon solar module can be enhanced by placing an array of microcylinders on top of the module glass. Photonic Mie-like resonances in the silica cylinders reduce infrared (IR) light reflection at the silica-air interface through engineered destructive interference of the resonant multipolar modes. By reciprocity, this improved anti-reflection effect increases the IR emissivity of the silica module glass. First, we studied the optimal emissivity profile for a typical silicon solar module that operates at elevated temperatures. By examining the thermal balance of a solar cell at T = 340 K, we found quartz silica to be the ideal module glass material due to its broad extinction coefficient in the λ = 3 - 30 µm spectral range. Subsequently, we designed a microcylinder array etched into the silica and optimized the dimensions for enhanced emissivity with FDTD simulations. The cylinder array is optimized to reduce the emissivity dip around λ = 9 µm that is caused by strong reflection at the silica-air interface.

Next, the microstructures were fabricated by UV photolithography and reactive ion etching into a silica substrate. To mimic a silicon solar module, we placed the microstructured silica substrate on a silicon substrate with a gold coating on the back. This stack has zero transmittance throughout the visible and IR wavelength ranges. The measured hemispherical IR reflectance compares very well to the simulated results, demonstrating the designed PRC enhancement. The fabricated microstructure increased the average emissivity between λ = 7.5 - 16 µm from 84.3% to 97.7%. Moreover, the microstructured silica substrate shows a slight increase in the transmittance in the spectral range where the Si solar cell absorbs. In conclusion, the flat silica substrate already achieves high PRC due to its near-ideal optical constants, realizing a cooling potential of 21 K compared to the bare silicon reference. The microcylinders decrease the equilibrium temperature by another 3 K. Assuming a 0.45% increase in efficiency per degree cooling, this would result in a relative efficiency increase of 1.35 – 10.8%, depending on the PRC capability of the reference module cover. This insight is also relevant for the development of light weight photovoltaics that do not use a glass cover.

These results highlight the opportunities of thermal management for photovoltaic applications by considering the module glass as an integral part of the photonic design. Our design concepts are general and applicable to all solar cell designs as well as module glass materials.

5.7 Methods

Passive radiative cooling calculation

In Figure 5.1, a schematic representation of the energy balance of a solar cell is shown, indicating the four main power terms that determine the cooling power of the cell:

$$P_{cool} = P_{rad} + P_{sun} + P_{atm} + P_{conv}. \tag{5.3}$$

Here, P_{sun} is the absorbed radiation coming from the sun, P_{atm} the absorbed thermal radiation from the atmosphere, P_{rad} the thermal radiation the solar cell is emitting, and P_{conv} the power lost or gained by convection. We assume that heat conduction via connection to the rooftop is negligible. The primary energy input is the irradiation from the sun, which is for normal incidence given by:

$$P_{sun} = -\int I_{AM1.5G}(\lambda)\alpha_{sc}(\lambda)d\lambda, \tag{5.4}$$

with $I_{AM1.5G}$ the solar irradiation within AM1.5G [11] and $\alpha(\lambda)$ the absorptivity of the solar cell. In Figure 5.2a, the AM1.5G solar spectrum is shown, and the silicon bandgap energy is indicated. The AM1.5G solar spectrum has an integrated power of 1000 Wm^{-2}, but silicon does not absorb light with energies below its bandgap. Therefore, for further calculations, P_{sun} is set to 808 Wm^{-2}, which is the integrated power in the AM1.5G solar spectrum for energies above the silicon bandgap (the yellow surface in Fig. 5.2a). The power input from the sun is completely independent of the infrared emissivity that is tuned to improve PRC. Therefore, this factor influences the absolute equilibrium temperatures but not the slope of the temperature curves in Figures 5.2d and 5.5b, nor the distance between different curves. For this comparative study, the precise value of P_{sun} is thus unimportant. This also allows us to neglect the fact that a solar cell converts about 20% of the incoming solar power into electricity rather than heat.

Secondly, heat can be exchanged between the solar cell and its environment through convection, given by the product of the non-radiative heat transfer coefficient (h_c) and the temperature difference between the solar cell and the ambient environment:

$$P_{conv}(T_{sc}, T_{amb}) = h_c\left(T_{sc} - T_{amb}\right). \tag{5.5}$$

We set the non-radiative heat transfer coefficient to 6 $Wm^{-2}K^{-1}$, corresponding to a wind speed of 1 m/s [187].

The solar cell radiates as a non-ideal blackbody, so its emitted radiative power is given by:

$$P_{rad}(T_{sc}) = \int I_{BB}(\lambda, T_{sc})\epsilon_{sc}(\lambda)d\lambda, \tag{5.6}$$

which is the product of the emissivity of the solar cell ($\epsilon_{sc}(\lambda)$), a number between zero and one that determines the quality of the solar cell as a blackbody, and the black body radiation according to Planck's law [203]:

$$I_{BB}(\lambda, T) = \frac{2hc^2}{\lambda^5}\frac{1}{e^{\frac{hc}{\lambda kT}} - 1}. \tag{5.7}$$

The atmosphere also radiates as a non-ideal blackbody. The radiative power from the atmosphere that is absorbed by the solar cell is given by:

$$P_{atm}(T_{amb}) = -\int I_{BB}(\lambda, T_{amb})\epsilon_{atm}(\lambda)\alpha_{sc}(\lambda)d\lambda, \tag{5.8}$$

which is the product of the blackbody radiation from the atmosphere, the emissivity of the atmosphere ($\epsilon_{\text{atm}}(\lambda)$), and the solar cell absorptivity ($\alpha_{\text{sc}}(\lambda)$). The blackbody spectrum of the atmosphere depends on the ambient temperature, T_{amb}, just as the blackbody spectrum of the sun depends on the temperature of its surface.

Then we use Kirchhoff's law for a body in thermal equilibrium, which states that the emissivity equals the absorptivity at every wavelength:

$$\epsilon(\lambda) = \alpha(\lambda). \tag{5.9}$$

Substituting the absorptivity for the emissivity in Eq. (5.8), we find that the cooling power depends on the balance between incoming radiation from the atmosphere and the outgoing blackbody radiation from the cell:

$$P_{cool}(T_{sc}, T_{amb}) \propto \int \left(I_{BB}(\lambda, T_{sc}) - I_{BB}(\lambda, T_{amb})\epsilon_{atm}(\lambda)\right)\epsilon_{sc}(\lambda)d\lambda. \tag{5.10}$$

Here, the emissivity of the atmosphere at normal incidence [187] is given by:

$$\epsilon_{atm}(\lambda) = 1 - T_{atm}(\lambda), \tag{5.11}$$

where $T_{\text{atm}}(\lambda)$ is the atmospheric transmittance [204, 205].

Both terms in Eq. (5.10) depend on the emissivity spectrum of the solar cell, $\epsilon_{\text{sc}}(\lambda)$, which is the most important parameter to tune to achieve PRC. The integrand in Eq. (5.10) scales linearly with $\epsilon_{\text{sc}}(\lambda)$, so the radiative cooling power can readily be optimized by calculating the integrand for each wavelength λ_{i}, at a given solar cell and ambient temperature. If the integrand is positive, i.e., at λ_{i} the solar cell emits more radiation than it receives from the atmosphere, the ideal emissivity $\epsilon_{\text{sc}}(\lambda_{\text{i}}) = 1$:

$$\begin{aligned} I_{BB}(\lambda_i, T_{sc}) - I_{BB}(\lambda_i, T_{amb})\epsilon_{atm}(\lambda_i) \geq 0; \qquad & \epsilon_{sc}(\lambda_i) = 1, \\ I_{BB}(\lambda_i, T_{sc}) - I_{BB}(\lambda_i, T_{amb})\epsilon_{atm}(\lambda_i) < 0; \qquad & \epsilon_{sc}(\lambda_i) = 0. \end{aligned} \tag{5.12}$$

In the case of a solar reflector, a body with a temperature equal to the ambient temperature ($T_{\text{sc}} = T_{\text{amb}}$), this criterion sets $\epsilon_{\text{sc}}(\lambda_{\text{i}}) = 1$ only for low atmospheric emissivity. This ideal curve is plotted in Figure 5.2c in green, where the emissivity is 1 only in the main atmospheric transmission window between 8 - 14 µm.

In the case of a solar absorber like a silicon solar cell, the operating temperature is higher than the ambient temperature ($T_{\text{sc}} > T_{\text{amb}}$). Figure 5.2b shows the atmospheric transmission with the blackbody spectra at temperatures 300 K and 340 K, corresponding to ambient temperature and the approximated temperature of an operating solar cell, respectively. Thus, the solar absorber emits more blackbody radiation than it receives from the atmosphere, independent of the atmospheric emissivity. Therefore, the ideal emissivity of a solar absorber is unity between λ = 3 - 30 µm, as plotted in blue in Fig. 5.2c. Below 3 µm, there is negligible blackbody radiation at 340 K, so we set the ideal solar absorber emissivity to 0 between λ = 3 µm and the solar cell bandgap.

The emissivity of the solar cell also equals its absorptivity (Kirchhoff's law, Eq. (5.9)), which can be determined by:

$$\epsilon_{sc}(\lambda) = \alpha_{sc}(\lambda) = 1 - R_{sc}(\lambda) - T_{sc}(\lambda), \tag{5.13}$$

with $R_{\text{sc}}(\lambda)$ the reflection and $T_{\text{sc}}(\lambda)$ the transmission of the solar cell. Maximizing the IR emissivity of the solar cell thus equals minimizing the reflection and transmission.

Transfer matrix model

We use a transfer matrix model based on the Fresnel equations to calculate the reflection and transmission of planar multilayer stacks. In particular, we use the Python implementation written by Steven J. Byrnes [206]. Literature values for the optical constants of Si and SiO_2 (Fig. 5.6) were used from ref. [74] and for Au from ref. [207].

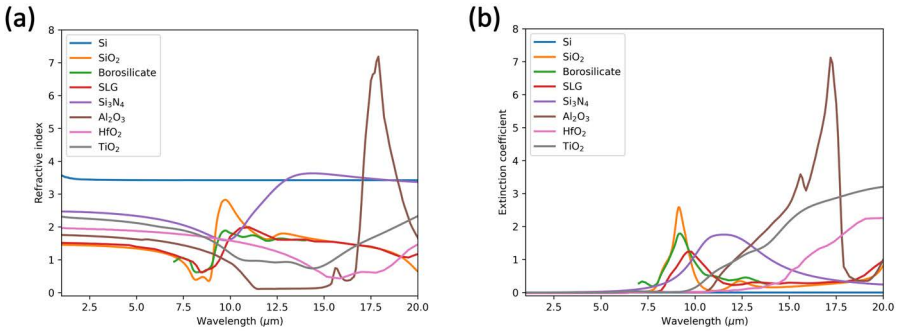

Figure 5.6: *(a) The refractive index and (b) the extinction coefficient of the most prevalent materials in photovoltaics.*

FDTD simulations

The optimization of the microcylinder array was performed by finite-difference time-domain (FDTD) calculations using Lumerical FDTD Solutions [72][48]. The single-pass IR reflection was minimized for a hexagonal array of silica cylinders at the interface of a semi-infinite silica substrate and air superstrate. Minimizing the reflection led to maximizing the cooling power (see calculation above), assuming that all IR light transmitted into the silica substrate is absorbed. The cylinder array was simulated in periodic boundary conditions. Convergence was found for a uniform 25 nm mesh size, conformal mesh refinement, and 10^{-7} auto shutoff value. The results of the optimization procedure are shown in Figure 5.7. The figure of merit is the radiative part of P_{cool}, according to Eq. (5.10), integrated between $\lambda = 2 - 16$ µm. In Figure 5.7a, we find a maximum for the pitch equal to 3.5 times the radius and height (equal). In Figure 5.7b, the pitch is constant at 3.5 times the radius, and we find the maximum for radius = 1.75 µm and height = 2.25 µm.

The multipole decomposition in Figure 5.3b was performed by calculating the electric field inside the microcylinder according to the method outlined by Evlyukhin et al. [38].

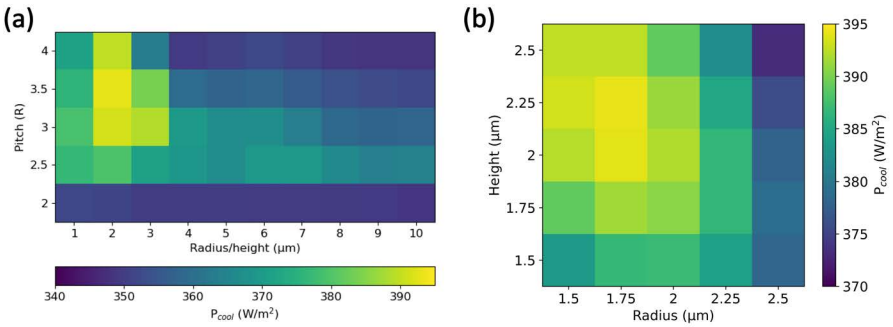

Figure 5.7: *Optimization of the hexagonal microcylinder array. (a) Pitch optimization as a function of radius and height (equal); maximum at pitch = 3.5 × radius. (b) Radius and height optimization, using optimal pitch found in (a). Optimal geometry was found at radius = 1.75 µm, height = 2.25 µm, and pitch = 3.5 × 1.75 = 6.125 µm. Color scaling is calculated according to Eq. (5.1).*

Electron-beam physical vapor deposition

A double-side polished (DSP) silicon wafer (WRS Materials, lightly phosphorus n-type doped, resistivity 1 - 20 Ωm) with a thickness of 500 µm was used as the absorber substrate. Electron-beam physical vapor deposition was used to deposit an 80 nm gold layer on one side of 24 × 24 mm^2 DSP Si substrates at a deposition rate of 0.5 Å/s.

UV photolithography and reactive ion etching

As a photolithography mask, a negative photoresist, ma-N 1420, was spin coated onto a 4 inch silica wafer of 500 µm thickness. A hexamethyldisilazane (HMDS) resist adhesion promotor was spin-coated on the wafer at 4000 RPM with 1000 RPM/s for 35 s, followed by a curing step on a 150 °C hot plate for 1 min. A 2 µm thick layer of ma-N 1420 was spin coated at 2000 RPM with 500 RPM/s for 30 s and cured at 100 °C for 2 min.

The photoresist was illuminated (λ = 365 nm) in a UV mask aligner (Süss MicroTec MABA6) through a quartz substrate with a chrome mask (commercial, Delta Mask BV). Unwanted interference due to reflection from the bottom silica-air interface is decreased by placing an absorptive tape on the back. The resist was developed by immersing the wafer into ma-D 533/S photoresist developer for 75 s; the wafer was then rinsed in H_2O for 30 s (twice) and blow-dried using a nitrogen gun.

The microstructured photoresist was used as a reactive ion etching (RIE) mask in an Oxford PlasmaPro Cobra RIE. A plasma of 50 sccm C_4F_8 and Ar gases was used to etch 2.20 µm deep in 16:30 min. The remaining photoresist was removed by immersion in base piranha, rinsed in H_2O, and dried under a nitrogen gun. Finally, the wafer is cut into 24 × 24 mm^2 substrates.

Infrared hemispherical reflection

The infrared hemispherical reflection measurements were conducted in a modified Bruker Vertex70 research-grade laboratory Fourier-transform infrared (FTIR) spectrometer at the University of Twente, as described in work by Hecker et al. [208] The Vertex70 is modified with an external, custom-made integrating sphere with a diffuse gold coating, with a Mercury Cadmium Telluride (MCT) infrared detector on top (λ = 1 - 16.7 μm). The sample is positioned at the south pole of the sphere, with a variable aperture of 20 mm. An external, high-power Globar source (λ = 1 - 16.7 μm) was used for high signal-to-noise measurements.

Measurements are taken at a wavenumber resolution of 8 cm^{-1} and repeated 8 times to average the noise. All measurements are normalized to the reflection of a diffuse or flat gold substrate, and the signal of an open sample port measurement is subtracted as background. The silica substrates were attached to the silicon substrate with immersion oil to avoid an air gap in between the substrates.

Visible to near-infrared hemispherical reflectance/transmittance

Hemispherical reflectance/transmittance measurements were conducted in the visible to near-infrared (NIR) wavelength ranges. An integrating sphere with a diffuse Teflon coating in reflection (transmission) configuration was used to capture all light reflecting from (transmitting through) the sample. An NKT SuperK Extreme EXU 6 supercontinuum laser was coupled into the integrating sphere, and the reflected (transmitted) light was measured with a grating spectrometer. In reflectance, the silica substrates were attached to the silicon substrate with immersion oil to avoid an air gap in between the substrates. The sample stacks were placed at the backside of the integrating sphere at an 8-degree angle from the optical path. In transmittance, only the silica substrates were placed in front of the integrating sphere.

The hemispherical reflectance/transmittance was measured over a wavelength range from 400 to 1562 nm in three intervals. In the visible (400-700 nm), the reflectance/transmittance was measured with 200 ms exposure time on a silicon CCD, using 150 grating lines per mm with a blaze of 500 nm. In the NIR (700-1050 and 1050-1562 nm), the exposure time was 1 second on an InGaAs detector, with 150 grating lines per mm and a blaze of 1200 nm. To exclude higher-order grating effects, all short-wavelength light was blocked, using a long-pass filter of 650 nm and 1050 nm for the 700-1050 nm and 1050-1562 nm wavelength range, respectively.

Bibliography

[1] J. Hecht, *City of Light: The Story of Fiber Optics*, revised ed. (Oxford University Press, 2004).

[2] D. Bardell, *The Biologists' Forum: The invention of the microscope,* BIOS **75**, 78 (2004).

[3] R. Feynman, R. Leighton, and M. Sands, *The Feynman Lectures on Physics, Vol. 1*, 50th ed. (Basic Books, 2011).

[4] United Nations, *Policy Briefs in Support of the High-Level Political Forum Leveraging Energy Action for Advancing the Sustainable Development Goals,* (2021).

[5] IEA, *Key World Energy Statistics*, Tech. Rep. (2021).

[6] S. Chu, Y. Cui, and N. Liu, *The path towards sustainable energy,* Nature Materials **16**, 16 (2016).

[7] B. Obama, *The irreversible momentum of clean energy,* Science **355**, 126 (2017).

[8] J. Nelson, *The Physics of Solar Cells*, 1st ed. (World Scientific Publishing Co., 2003).

[9] U. Wurfel, A. Cuevas, and P. Wurfel, *Charge carrier separation in solar cells,* IEEE Journal of Photovoltaics **5**, 461 (2015).

[10] D. Goldsmith and T. Owen, *The Search For Life In The Universe*, 3rd ed. (University Science Books, 2001).

[11] Subcommittee 09, *Standard Tables for Reference Solar Spectral Irradiances: Direct Normal and Hemispherical on 37° Tilted Surface,* in *Book of Standards Volume 14.04* (ASTM International, 2020).

[12] W. Shockley and H. J. Queisser, *Detailed Balance Limit of Efficiency of p-n Junction Solar Cells,* Journal of Applied Physics **32**, 510 (1961).

[13] A. Polman, M. Knight, E. C. Garnett, B. Ehrler, and W. C. Sinke, *Photovoltaic materials: Present efficiencies and future challenges,* Science **352**, 307 (2016).

[14] U.S. Energy Information Administration, *Average Operating Heat Rate for Selected Energy Sources,* (2021).

[15] W. C. Sinke, *Development of photovoltaic technologies for global impact,* Renewable Energy **138**, 911 (2019).

[16] M. Yamaguchi, K.-H. Lee, P. Schygulla, F. Dimroth, T. Takamoto, R. Ozaki, K. Nakamura, N. Kojima, and Y. Ohshita, *Approaches for High-Efficiency III-V/Si Tandem Solar Cells,* Energy and Power Engineering **13**, 413 (2021).

[17] E. C. Warmann, P. Espinet-Gonzalez, N. Vaidya, S. Loke, A. Naqavi, T. Vinogradova, M. Kelzenberg, C. Leclerc, E. Gdoutos, S. Pellegrino, and H. A. Atwater, *An ultralight concentrator photovoltaic system for space solar power harvesting,* Acta Astronautica **170**, 443 (2020).

[18] ITRPV, *International technology roadmap for photovoltaic*, Tech. Rep. (2020).

[19] J. S. Van Der Burgt and E. C. Garnett, *Nanophotonic Emission Control for Improved Photovoltaic Efficiency,* ACS Photonics **7**, 1589 (2020).

[20] B. Ehrler, E. Alarcón-Lladó, S. W. Tabernig, T. Veeken, E. C. Garnett, and A. Polman, *Photovoltaics Reaching for the Shockley–Queisser Limit,* ACS Energy Letters **5**, 3029 (2020).

[21] J. Perlin, *Let it shine* (New World Library, 2013).

[22] M. A. Green, Y. Hishikawa, W. Warta, E. D. Dunlop, D. H. Levi, J. Hohl-Ebinger, and A. W. Ho-Baillie, *Solar cell efficiency tables (version 50),* Progress in Photovoltaics: Research and Applications **25**, 668 (2017).

[23] M. F. Ashby, P. J. Ferreira, and D. L. Schodek, *An Evolutionary Perspective,* in *Nanomaterials, Nanotechnologies and Design* (Elsevier, 2009) pp. 17–39.

[24] A. Cordaro, J. Van De Groep, S. Raza, E. F. Pecora, F. Priolo, and M. L. Brongersma, *Antireflection High-Index Metasurfaces Combining Mie and Fabry-Pérot Resonances,* ACS Photonics **6**, 453 (2019).

[25] G. Mie, *Beiträge zur Optik trüber Medien, speziell kolloidaler Metallösungen,* Annalen der Physik **330**, 377 (1908).

[26] P. Spinelli, M. A. Verschuuren, and A. Polman, *Broadband omnidirectional antireflection coating based on subwavelength surface Mie resonators,* Nature Communications **3**, 692 (2012).

[27] H. A. Atwater and A. Polman, *Plasmonics for improved photovoltaic devices,* Nature Materials **9**, 205 (2010).

[28] M. A. van de Haar, R. Maas, B. Brenny, and A. Polman, *Surface plasmon polariton modes in coaxial metal-dielectric-metal waveguides,* New Journal of Physics **18**, 043016 (2016).

[29] A. Polman and H. A. Atwater, *Photonic design principles for ultrahigh-efficiency photovoltaics,* Nature Materials **11**, 174 (2012).

[30] A. I. Kuznetsov, A. E. Miroshnichenko, M. L. Brongersma, Y. S. Kivshar, and B. Luk'yanchuk, *Optically resonant dielectric nanostructures,* Science **354**, 846 (2016).

[31] M. C. Van Lare and A. Polman, *Optimized Scattering Power Spectral Density of Photovoltaic Light-Trapping Patterns,* ACS Photonics **2**, 822 (2015).

[32] E. C. Garnett, B. Ehrler, A. Polman, and E. Alarcon-Llado, *Photonics for Photovoltaics: Advances and Opportunities,* ACS Photonics **8**, 61 (2021).

[33] IEA, *World Energy Outlook 2021,* (2021).

[34] M. Kryszak and L. W. Wang, *The value of aesthetics in the BIPV roof products segment: a multiperspective study under European market conditions,* Energy Sources, Part A: Recovery, Utilization, and Environmental Effects (2020), 10.1080/15567036.2020.1807656.

[35] T. E. Kuhn, C. Erban, M. Heinrich, J. Eisenlohr, F. Ensslen, and D. H. Neuhaus, *Review of technological design options for building integrated photovoltaics (BIPV),* Energy and Buildings **231**, 110381 (2021).

[36] V. Neder, S. L. Luxembourg, and A. Polman, *Efficient colored silicon solar modules using integrated resonant dielectric nanoscatterers,* Applied Physics Letters **111**, 073902 (2017).

[37] B. Blasi, T. Kroyer, T. Kuhn, and O. Hohn, *The MorphoColor Concept for Colored Photovoltaic Modules,* IEEE Journal of Photovoltaics **11**, 1305 (2021).

[38] G. Lozano, S. R. Rodriguez, M. A. Verschuuren, and J. Gómez Rivas, *Metallic nanostructures for efficient LED lighting,* Light: Science & Applications **5**, e16080 (2016).

[39] E. Khaidarov, Z. Liu, R. Paniagua-Domínguez, S. T. Ha, V. Valuckas, X. Liang, Y. Akimov, P. Bai, C. E. Png, H. V. Demir, and A. I. Kuznetsov, *Control of LED Emission with Functional Dielectric Metasurfaces,* Laser and Photonics Reviews **14**, 1 (2020).

[40] G. Lozano, D. J. Louwers, S. R. Rodríguez, S. Murai, O. T. Jansen, M. A. Verschuuren, and J. Gómez Rivas, *Plasmonics for solid-state lighting: enhanced excitation and directional emission of highly efficient light sources,* Light: Science & Applications **2**, e66 (2013).

[41] F. Prins, D. K. Kim, J. Cui, E. De Leo, L. L. Spiegel, K. M. McPeak, and D. J. Norris, *Direct Patterning of Colloidal Quantum-Dot Thin Films for Enhanced and Spectrally Selective Out-Coupling of Emission,* Nano Letters **17**, 1319 (2017).

[42] N. D. Bronstein, Y. Yao, L. Xu, E. O'Brien, A. S. Powers, V. E. Ferry, A. P. Alivisatos, and R. G. Nuzzo, *Quantum Dot Luminescent Concentrator Cavity Exhibiting 30-fold Concentration,* ACS Photonics **2**, 1576 (2015).

[43] N. D. Bronstein, L. Li, L. Xu, Y. Yao, V. E. Ferry, A. P. Alivisatos, and R. G. Nuzzo, *Luminescent solar concentration with semiconductor nanorods and transfer-printed micro-silicon solar cells,* ACS Nano **8**, 44 (2014).

[44] N. J. Thompson, M. W. B. Wilson, D. N. Congreve, P. R. Brown, J. M. Scherer, T. Bischof, M. Wu, N. Geva, M. Welborn, T. V. Voorhis, V. Bulović, M. G. Bawendi, and M. Baldo, *Energy harvesting of non-emissive triplet excitons in tetracene by emissive PbS nanocrystals,* Nature Materials **13**, 1039 (2014).

[45] C. Ye, S. Chen, J. Liao, Y. S. Zhang, X. Wang, and Y. Song, *Efficiently Enhanced Triplet–Triplet Annihilation Upconversion Boosted by Multibandgaps Photonic Crystals,* The Journal of Physical Chemistry C **124**, 18482 (2020).

[46] N. V. Hoang, A. Pereira, H. S. Nguyen, E. Drouard, B. Moine, T. Deschamps, R. Orobtchouk, A. Pillonnet, and C. Seassal, *Giant Enhancement of Luminescence Down-Shifting by a Doubly Resonant Rare-Earth-Doped Photonic Metastructure,* ACS Photonics **4**, 1705 (2017), arXiv:1303.4151 .

[47] N. J. Davis, J. R. Allardice, J. Xiao, A. J. Petty, N. C. Greenham, J. E. Anthony, and A. Rao, *Singlet Fission and Triplet Transfer to PbS Quantum Dots in TIPS-Tetracene Carboxylic Acid Ligands,* Journal of Physical Chemistry Letters **9**, 1454 (2018).

[48] H. Mertens, J. S. Biteen, H. A. Atwater, and A. Polman, *Polarization-Selective Plasmon-Enhanced Silicon Quantum-Dot Luminescence,* Nano Letters **6**, 2622 (2006).

[49] H. Mertens and A. Polman, *Plasmon-enhanced erbium luminescence,* Applied Physics Letters **89**, 1 (2006).

[50] A. G. Curto, G. Volpe, T. H. Taminiau, M. P. Kreuzer, R. Quidant, and N. F. van Hulst, *Unidirectional Emission of a Quantum Dot Coupled to a Nanoantenna,* Science **329**, 930 (2010).

[51] T. Kosako, Y. Kadoya, and H. F. Hofmann, *Directional control of light by a nano-optical Yagi-Uda antenna,* Nature Photonics **4**, 312 (2010).

[52] T. Coenen, F. Bernal Arango, A. Femius Koenderink, and A. Polman, *Directional emission from a single plasmonic scatterer,* Nature Communications **5**, 1 (2014).

[53] T. Shegai, S. Chen, V. D. Miljković, G. Zengin, P. Johansson, and M. Käll, *A bimetallic nanoantenna for directional colour routing,* Nature Communications **2**, 481 (2011).

[54] J. van de Groep and A. Polman, *Designing dielectric resonators on substrates: Combining magnetic and electric resonances,* Optics Express **21**, 26285 (2013).

[55] I. Staude, A. E. Miroshnichenko, M. Decker, N. T. Fofang, S. Liu, E. Gonzales, J. Dominguez, T. S. Luk, D. N. Neshev, I. Brener, and Y. Kivshar, *Tailoring directional scattering through magnetic and electric resonances in subwavelength silicon nanodisks,* ACS Nano **7**, 7824 (2013).

[56] Y. H. Fu, A. I. Kuznetsov, A. E. Miroshnichenko, Y. F. Yu, and B. Luk'yanchuk, *Directional visible light scattering by silicon nanoparticles.* Nature Communications **4**, 1527 (2013).

[57] Y. Yang, A. E. Miroshnichenko, S. V. Kostinski, M. Odit, P. Kapitanova, M. Qiu, and Y. S. Kivshar, *Multimode directionality in all-dielectric metasurfaces,* Physical Review B **95**, 165426 (2017).

[58] A. Capretti, A. Lesage, and T. Gregorkiewicz, *Integrating Quantum Dots and Dielectric Mie Resonators: A Hierarchical Metamaterial Inheriting the Best of Both,* ACS Photonics **4**, 2187 (2017).

[59] A. F. Cihan, A. G. Curto, S. Raza, P. G. Kik, and M. L. Brongersma, *Silicon Mie resonators for highly directional light emission from monolayer MoS2,* Nature Photonics **12**, 284 (2018).

[60] I. Staude, V. V. Khardikov, N. T. Fofang, S. Liu, M. Decker, D. N. Neshev, T. S. Luk, I. Brener, and Y. S. Kivshar, *Shaping Photoluminescence Spectra with Magnetoelectric Resonances in All-Dielectric Nanoparticles,* ACS Photonics **2**, 172 (2015).

[61] A. Vaskin, S. Liu, S. Addamane, P. P. Vabishchevich, Y. Yang, G. Balarishnan, M. B. Sinclair, T. Pertsch, I. Brener, and I. Staude, *Manipulation of quantum dot emission with semiconductor metasurfaces exhibiting magnetic quadrupole resonances,* Optics Express **29**, 5567 (2021).

[62] S. Murai, G. W. Castellanos, T. V. Raziman, A. G. Curto, and J. G. Rivas, *Enhanced Light Emission by Magnetic and Electric Resonances in Dielectric Metasurfaces,* Advanced Optical Materials **8**, 1902024 (2020).

[63] H. Agrawal and E. C. Garnett, *Nanocube Imprint Lithography,* ACS Nano **14**, 11009 (2020).

[64] A. Gopal, K. Hoshino, and X. Zhang, *Nano-stamping of quantum dot based inorganic light emitting devices,* in *2009 IEEE/LEOS International Conference on Optical MEMS and Nanophotonics*, Figure 4 (IEEE, 2009) pp. 85–86.

[65] M. K. Choi, J. Yang, K. Kang, D. C. Kim, C. Choi, C. Park, S. J. Kim, S. I. Chae, T. H. Kim, J. H. Kim, T. Hyeon, and D. H. Kim, *Wearable red-green-blue quantum dot light-emitting diode array using high-resolution intaglio transfer printing,* Nature Communications **6**, 1 (2015).

[66] T. H. Kim, K. S. Cho, E. K. Lee, S. J. Lee, J. Chae, J. W. Kim, D. H. Kim, J. Y. Kwon, G. Amaratunga, S. Y. Lee, B. L. Choi, Y. Kuk, J. M. Kim, and K. Kim, *Full-colour quantum dot displays fabricated by transfer printing,* Nature Photonics **5**, 176 (2011).

[67] S. Oh, S. K. Park, J. H. Kim, I. Cho, H. J. Kim, and S. Y. Park, *Patterned Taping: A High-Efficiency Soft Lithographic Method for Universal Thin Film Patterning,* ACS Nano **10**, 3478 (2016).

[68] L. Novotny and B. Hecht, *Principles of Nano-Optics*, 2nd ed. (Cambridge University Press, Cambridge, 2012).

[69] E. Snoeks, A. Lagendijk, and A. Polman, *Measuring and Modifying the Spontaneous Emission Rate of Erbium near an Interface,* Physical Review Letters **74**, 2459 (1995).

[70] K. Drexhage, *Influence of a dielectric interface on fluorescence decay time,* Journal of Luminescence **1-2**, 693 (1970).

[71] A. B. Evlyukhin, T. Fischer, C. Reinhardt, and B. N. Chichkov, *Optical theorem and multipole scattering of light by arbitrarily shaped nanoparticles,* Physical Review B **94**, 1 (2016).

[72] ANSYS Lumerical, *FDTD Solutions,* (2022).

[73] J. Yang, J. P. Hugonin, and P. Lalanne, *Near-to-Far Field Transformations for Radiative and Guided Waves,* ACS Photonics **3**, 395 (2016).

[74] E. D. Palik, *Handbook of Optical Constants of Solids*, 1st ed., Vol. 1 (Academic Press, 1997).

[75] G. J. Brakenhoff, K. Visscher, and H. T. M. van der Voort, *Size and Shape of The Confocal Spot: Control and Relation to 3D Imaging and Image Processing,* in *Handbook of Biological Confocal Microscopy* (Springer US, Boston, MA, 1990) pp. 87–91.

[76] Wolfram, *Mathematica,* (2020).

[77] BP, *BP Statistical Review of World Energy*, Tech. Rep. (2019).

[78] Enerdata, *Global Energy Statistical Yearbook,* (2019).

[79] M. Meir, *IEA EBC Annex 58,* Tech. Rep. (IEA Solar Heating and Cooling Programme, 2019).

[80] R. J. Yang and P. X. Zou, *Building integrated photovoltaics (BIPV): costs, benefits, risks, barriers and improvement strategy,* International Journal of Construction Management **16**, 39 (2016).

[81] R. R. Lunt and V. Bulovic, *Transparent, near-infrared organic photovoltaic solar cells for window and energy-scavenging applications,* Applied Physics Letters **98**, 113305 (2011).

[82] C. J. Traverse, R. Pandey, M. C. Barr, and R. R. Lunt, *Emergence of highly transparent photovoltaics for distributed applications,* Nature Energy **2**, 849 (2017).

[83] A. A. Husain, W. Z. W. Hasan, S. Shafie, M. N. Hamidon, and S. S. Pandey, *A review of transparent solar photovoltaic technologies,* Renewable and Sustainable Energy Reviews **94**, 779 (2018).

[84] C. Lamnatou and D. Chemisana, *Solar radiation manipulations and their role in greenhouse claddings: Fluorescent solar concentrators, photoselective and other materials,* Renewable and Sustainable Energy Reviews **27**, 175 (2013).

[85] W. H. Weber and J. Lambe, *Luminescent greenhouse collector for solar radiation,* Applied Optics **15**, 2299 (1976).

[86] C. Corrado, S. W. Leow, M. Osborn, I. Carbone, K. Hellier, M. Short, G. Alers, and S. A. Carter, *Power generation study of luminescent solar concentrator greenhouse,* Journal of Renewable and Sustainable Energy **8**, 043502 (2016).

[87] M. E. Loik, S. A. Carter, G. Alers, C. E. Wade, D. Shugar, C. Corrado, D. Jokerst, and C. Kitayama, *Wavelength-Selective Solar Photovoltaic Systems: Powering Greenhouses for Plant Growth at the Food-Energy-Water Nexus,* Earth's Future **5**, 1044 (2017).

[88] E. Cuce, D. Harjunowibowo, and P. M. Cuce, *Renewable and sustainable energy saving strategies for greenhouse systems: A comprehensive review,* Renewable and Sustainable Energy Reviews **64**, 34 (2016).

[89] R. Fu, D. Feldman, R. Margolis, M. Woodhouse, K. Ardani, R. Fu, D. Feldman, R. Margolis, M. Woodhouse, and K. Ardani, *NREL Technical Report*, Tech. Rep. (National Renewable Energy Laboratory, 2018).

[90] W. Shurcliff and C. R. Jones, *The Trapping of Fluorescent Light Produced within Objects of High Geometrical Symmetry,* Journal of the Optical Society of America **39**, 912 (1949).

[91] E. Yablonovitch, *Thermodynamics of the fluorescent planar concentrator,* Journal of the Optical Society of America **70**, 1362 (1980).

[92] A. Rabl, *Comparison of solar concentrators,* Solar Energy **18**, 93 (1976).

[93] M. G. Debije and V. A. Rajkumar, *Direct versus indirect illumination of a prototype luminescent solar concentrator,* Solar Energy **122**, 334 (2015).

[94] Y. Li, Y. Sun, and Y. Zhang, *Luminescent solar concentrators performing under different light conditions,* Solar Energy **188**, 1248 (2019).

[95] V. A. Rajkumar, C. Weijers, and M. G. Debije, *Distribution of absorbed heat in luminescent solar concentrator lightguides and effect on temperatures of mounted photovoltaic cells,* Renewable Energy **80**, 308 (2015).

[96] A. Reinders, R. Kishore, L. Slooff, and W. Eggink, *Luminescent solar concentrator photovoltaic designs,* (2018).

[97] P. Moraitis, G. van Leeuwen, and W. van Sark, *Visual appearance of nanocrystal-based luminescent solar concentrators,* Materials **16** (2019), 10.3390/ma12060885.

[98] F. Meinardi, F. Bruni, and S. Brovelli, *Luminescent solar concentrators for building-integrated photovoltaics,* Nature Reviews Materials **2**, 1 (2017).

[99] A. Reinders, M. G. Debije, and A. Rosemann, *Measured Efficiency of a Luminescent Solar Concentrator PV Module Called Leaf Roof,* IEEE Journal of Photovoltaics **7**, 1663 (2017).

[100] J. A. H. P. Sol, G. H. Timmermans, A. J. van Breugel, A. P. H. J. Schenning, and M. G. Debije, *Multistate Luminescent Solar Concentrator "Smart" Windows,* Advanced Energy Materials **8**, 1702922 (2018).

[101] K. Wu, H. Li, and V. I. Klimov, *Tandem luminescent solar concentrators based on engineered quantum dots,* Nature Photonics **12**, 105 (2018).

[102] D. R. Needell, O. Ilic, C. R. Bukowsky, Z. Nett, L. Xu, J. He, H. Bauser, B. G. Lee, J. F. Geisz, R. G. Nuzzo, A. P. Alivisatos, and H. A. Atwater, *Design Criteria for Micro-Optical Tandem Luminescent Solar Concentrators,* IEEE Journal of Photovoltaics **8**, 1560 (2018).

[103] D. R. Needell, Z. Nett, O. Ilic, C. R. Bukowsky, J. He, L. Xu, R. G. Nuzzo, B. G. Lee, J. F. Geisz, A. P. Alivisatos, and H. A. Atwater, *Micro-optical Tandem Luminescent Solar Concentrator,* in *2017 IEEE 44th Photovoltaic Specialist Conference (PVSC)* (IEEE, 2017) pp. 1737–1740.

[104] D. R. Needell, C. R. Bukowsky, S. Darbe, H. Bauser, O. Ilic, and H. A. Atwater, *Spectrally Matched Quantum Dot Photoluminescence in GaAs-Si Tandem Luminescent Solar Concentrators,* IEEE Journal of Photovoltaics **9**, 1 (2019).

[105] M. M. Lunardi, D. R. Needell, H. Bauser, M. Phelan, H. A. Atwater, and R. Corkish, *Life Cycle Assessment of tandem LSC-Si devices,* Energy **181**, 1 (2019).

[106] M. G. Debije and P. P. C. Verbunt, *Thirty Years of Luminescent Solar Concentrator Research: Solar Energy for the Built Environment,* Advanced Energy Materials **2**, 12 (2012).

[107] A. Goetzberger and W. Greube, *Solar energy conversion with fluorescent collectors,* Applied Physics **14**, 123 (1977).

[108] C. Tummeltshammer, A. Taylor, A. Kenyon, and I. Papakonstantinou, *Losses in luminescent solar concentrators unveiled,* Solar Energy Materials and Solar Cells **144**, 40 (2016).

[109] A. R. Burgers, L. H. Slooff, R. Kinderman, and J. M. van Roosmalen, *Modeling of Luminescent Concentrators by Ray-tracing,* in *Proceedings of Twentieth European Photovoltaic Solar Energy Conference* (2005) pp. 394–397.

[110] B. Rowan, L. Wilson, and B. Richards, *Advanced Material Concepts for Luminescent Solar Concentrators,* IEEE Journal of Selected Topics in Quantum Electronics **14**, 1312 (2008).

[111] A. L. Martínez and D. Gómez, *Design, fabrication, and characterization of a luminescent solar concentrator with optimized optical concentration through minimization of optical losses,* Journal of Photonics for Energy **6**, 045504 (2016).

[112] Z. Krumer, W. G. van Sark, R. E. Schropp, and C. de Mello Donegá, *Compensation of self-absorption losses in luminescent solar concentrators by increasing luminophore concentration,* Solar Energy Materials and Solar Cells **167**, 133 (2017).

[113] A. Kerrouche, D. Hardy, D. Ross, and B. Richards, *Luminescent solar concentrators: From experimental validation of 3D ray-tracing simulations to coloured stained-glass windows for BIPV,* Solar Energy Materials and Solar Cells **122**, 99 (2014).

[114] R. Connell, C. Pinnell, and V. E. Ferry, *Designing spectrally-selective mirrors for use in luminescent solar concentrators,* Journal of Optics **20**, 024009 (2018).

[115] L. H. Slooff, E. E. Bende, A. R. Burgers, T. Budel, M. Pravettoni, R. P. Kenny, E. D. Dunlop, and A. Büchtemann, *A Luminescent Solar Concentrator with 7.1% power conversion efficiency,* Physica Status Solidi - Rapid Research Letters **2**, 257 (2008).

[116] M. G. Debije, R. C. Evans, and G. Griffini, *Laboratory protocols for measuring and reporting the performance of luminescent solar concentrators,* Energy & Environmental Science **14**, 293 (2021).

[117] L. Xu, Y. Yao, N. D. Bronstein, L. Li, A. P. Alivisatos, and R. G. Nuzzo, *Enhanced Photon Collection in Luminescent Solar Concentrators with Distributed Bragg Reflectors,* ACS Photonics **3**, 278 (2016).

[118] D. K. G. de Boer, D. J. Broer, M. G. Debije, W. Keur, A. Meijerink, C. R. Ronda, and P. P. C. Verbunt, *Progress in phosphors and filters for luminescent solar concentrators,* Optics Express **20**, A395 (2012).

[119] D. K. G. de Boer, C.-W. Lin, M. P. Giesbers, H. J. Cornelissen, M. G. Debije, P. P. C. Verbunt, and D. J. Broer, *Polarization-independent filters for luminescent solar concentrators,* Applied Physics Letters **98**, 021111 (2011).

[120] C. Tummeltshammer, A. Taylor, A. J. Kenyon, and I. Papakonstantinou, *Homeotropic alignment and Förster resonance energy transfer: The way to a brighter luminescent solar concentrator,* Journal of Applied Physics **116**, 173103 (2014).

[121] M. G. Debije, *Solar Energy Collectors with Tunable Transmission,* Advanced Functional Materials **20**, 1498 (2010).

[122] C. L. Mulder, P. D. Reusswig, A. P. Beyler, H. Kim, C. Rotschild, and M. A. Baldo, *Dye alignment in luminescent solar concentrators: II Horizontal alignment for energy harvesting in linear polarizers,* Optics Express **18**, A91 (2010).

[123] H. C. Bauser, C. R. Bukowsky, M. Phelan, W. Weigand, D. R. Needell, Z. C. Holman, and H. A. Atwater, *Photonic Crystal Waveguides for >90% Light Trapping Efficiency in Luminescent Solar Concentrators,* ACS Photonics **7**, 2122 (2020).

[124] P. P. C. Verbunt, C. Sánchez-Somolinos, D. J. Broer, and M. G. Debije, *Anisotropic light emissions in luminescent solar concentrators–isotropic systems,* Optics Express **21**, A485 (2013).

[125] P. P. C. Verbunt, T. M. de Jong, D. K. de Boer, D. J. Broer, and M. G. Debije, *Anisotropic light emission from aligned luminophores,* The European Physical Journal Applied Physics **67**, 10201 (2014).

[126] P. P. C. Verbunt, A. Kaiser, K. Hermans, C. W. M. Bastiaansen, D. J. Broer, and M. G. Debije, *Controlling Light Emission in Luminescent Solar Concentrators Through Use of Dye Molecules Aligned in a Planar Manner by Liquid Crystals,* Advanced Functional Materials **19**, 2714 (2009).

[127] P. Moraitis, D. K. G. de Boer, P. T. Prins, C. de Mello Donegá, K. Neyts, and W. G. J. H. M. van Sark, *Should Anisotropic Emission or Reabsorption of Nanoparticle Luminophores Be Optimized for Increasing Luminescent Solar Concentrator Efficiency?* Solar RRL **4**, 2000279 (2020).

[128] D. A. Hanifi, N. D. Bronstein, B. A. Koscher, Z. Nett, J. K. Swabeck, K. Takano, A. M. Schwartzberg, L. Maserati, K. Vandewal, Y. van de Burgt, A. Salleo, and A. P. Alivisatos, *Redefining near-unity luminescence in quantum dots with photothermal threshold quantum yield,* Science **363**, 1199 (2019).

[129] H. Fang, C. Battaglia, C. Carraro, S. Nemsak, B. Ozdol, J. S. Kang, H. A. Bechtel, S. B. Desai, F. Kronast, A. A. Unal, G. Conti, C. Conlon, G. K. Palsson, M. C. Martin, A. M. Minor, C. S. Fadley, E. Yablonovitch, R. Maboudian, and A. Javey, *Strong interlayer coupling in van der Waals heterostructures built from single-layer chalcogenides,* Proceedings of the National Academy of Sciences **111**, 6198 (2014).

[130] M. A. Steiner, J. F. Geisz, I. García, D. J. Friedman, A. Duda, and S. R. Kurtz, *Optical enhancement of the open-circuit voltage in high quality GaAs solar cells,* Journal of Applied Physics **113**, 123109 (2013).

[131] M. A. Green, *Radiative efficiency of state-of-the-art photovoltaic cells,* Progress in Photovoltaics: Research and Applications **20**, 472 (2012).

[132] S. Sandhu, Z. Yu, and S. Fan, *Detailed balance analysis of nanophotonic solar cells,* Optics Express **21**, 1209 (2013).

[133] L. H. Slooff, R. Kinderman, A. R. Burgers, A. Büchtemann, R. Danz, T. B. Meyer, A. J. Chatten, D. Farell, K. W. J. Barnham, and J. A. M. van Roosmalen, *The luminescent concentrator illuminated,* in *Proceedings of SPIE, Photonics for Solar Energy Systems*, Vol. 6197 (2006) p. 61970K.

[134] U. Rau, F. Einsele, and G. C. Glaeser, *Efficiency limits of photovoltaic fluorescent collectors,* Applied Physics Letters **87**, 171101 (2005).

[135] G. C. Glaeser and U. Rau, *Collection and conversion properties of photovoltaic fluorescent collectors with photonic band stop filters,* in *Photonics for Solar Energy Systems*, Vol. 6197 (2006) p. 61970L.

[136] D. Şahin, B. Ilan, and D. F. Kelley, *Monte-Carlo simulations of light propagation in luminescent solar concentrators based on semiconductor nanoparticles,* Journal of Applied Physics **110**, 033108 (2011).

[137] S. Sadeghi, R. Melikov, H. Bahmani Jalali, O. Karatum, S. B. Srivastava, D. Conkar, E. N. Firat-Karalar, and S. Nizamoglu, *Ecofriendly and Efficient Luminescent Solar Concentrators Based on Fluorescent Proteins,* ACS Applied Materials & Interfaces **11**, 8710 (2019).

[138] A. H. Smets, K. Jäger, O. Isabella, R. A. van Swaaij, and M. Zeman, *Solar Energy: The Physics and Engineering of Photovoltaic Conversion, Technologies and Systems* (UIT Cambridge Ltd., 2016).

[139] Enerdata, *Global Energy Statistical Yearbook,* (2021).

[140] O. Almora, D. Baran, G. C. Bazan, C. Berger, C. I. Cabrera, K. R. Catchpole, S. Erten-Ela, F. Guo, J. Hauch, A. W. Ho-Baillie, T. J. Jacobsson, R. A. Janssen, T. Kirchartz, N. Kopidakis, Y. Li, M. A. Loi, R. R. Lunt, X. Mathew, M. D. McGehee, J. Min, D. B. Mitzi, M. K. Nazeeruddin, J. Nelson, A. F. Nogueira, U. W. Paetzold, N. G. Park, B. P. Rand, U. Rau, H. J. Snaith, E. Unger, L. Vaillant-Roca, H. L. Yip, and C. J. Brabec, *Device Performance of Emerging Photovoltaic Materials (Version 1),* Advanced Energy Materials **11**, 2002774 (2021).

[141] M. R. Bergren, N. S. Makarov, K. Ramasamy, A. Jackson, R. Guglielmetti, and H. McDaniel, *High-Performance CuInS2 Quantum Dot Laminated Glass Luminescent Solar Concentrators for Windows,* ACS Energy Letters **3**, 520 (2018).

[142] A. Renny, C. Yang, R. Anthony, and R. R. Lunt, *Luminescent Solar Concentrator Paintings: Connecting Art and Energy,* Journal of Chemical Education **95**, 1161 (2018).

[143] E. Mengelkamp, B. Notheisen, C. Beer, D. Dauer, and C. Weinhardt, *A blockchain-based smart grid: towards sustainable local energy markets,* Computer Science - Research and Development **33**, 207 (2018).

[144] C. Yang, D. Liu, M. Bates, M. C. Barr, and R. R. Lunt, *How to Accurately Report Transparent Solar Cells,* Joule **3**, 1803 (2019).

[145] J. S. Van Der Burgt, D. R. Needell, T. Veeken, A. Polman, E. C. Garnett, and H. A. Atwater, *Unlocking Higher Power Efficiencies in Luminescent Solar Concentrators through Anisotropic Luminophore Emission,* ACS Applied Materials and Interfaces **13**, 40742 (2021).

[146] G. Smestad, H. Ries, R. Winston, and E. Yablonovitch, *The thermodynamic limits of light concentrators,* Solar Energy Materials **21**, 99 (1990).

[147] F. Meinardi, S. Ehrenberg, L. Dhamo, F. Carulli, M. Mauri, F. Bruni, R. Simonutti, U. Kortshagen, and S. Brovelli, *Highly efficient luminescent solar concentrators based on earth-Abundant indirect-bandgap silicon quantum dots,* Nature Photonics **11**, 177 (2017).

[148] K. E. Knowles, T. B. Kilburn, D. G. Alzate, S. McDowall, and D. R. Gamelin, *Bright CuInS2 /CdS nanocrystal phosphors for high-gain full-spectrum luminescent solar concentrators,* Chemical Communications **51**, 9129 (2015).

[149] J. Roncali, *Luminescent Solar Collectors: Quo Vadis?* Advanced Energy Materials **10**, 2001907 (2020).

[150] G. C. Heres, L. M. Einhaus, and R. Saive, *Analytical Model for the Performance of a Free-Space Luminescent Solar Concentrator,* in *2021 IEEE 48th Photovoltaic Specialists Conference (PVSC)* (IEEE, 2021) pp. 1027–1029.

[151] L. R. Bradshaw, K. E. Knowles, S. McDowall, and D. R. Gamelin, *Nanocrystals for Luminescent Solar Concentrators,* Nano Letters **15**, 1315 (2015).

[152] M. Fisher, D. Farrell, M. Zanella, A. Lupi, P. N. Stavrinou, and A. J. Chatten, *Utilizing vertically aligned CdSe/CdS nanorods within a luminescent solar concentrator,* Applied Physics Letters **106**, 3 (2015).

[153] A. Vaskin, R. Kolkowski, A. F. Koenderink, and I. Staude, *Light-emitting metasurfaces,* Nanophotonics **8**, 1151 (2019).

[154] A. G. Curto, T. H. Taminiau, G. Volpe, M. P. Kreuzer, R. Quidant, and N. F. van Hulst, *Multipolar radiation of quantum emitters with nanowire optical antennas,* Nature Communications **4**, 1750 (2013).

[155] S. R. K. Rodriguez, F. B. Arango, T. P. Steinbusch, M. A. Verschuuren, A. F. Koenderink, and J. G. Rivas, *Breaking the Symmetry of Forward-Backward Light Emission with Localized and Collective Magnetoelectric Resonances in Arrays of Pyramid-Shaped Aluminum Nanoparticles,* Physical Review Letters **113**, 247401 (2014).

[156] I. Staude, T. Pertsch, and Y. S. Kivshar, *All-Dielectric Resonant Meta-Optics Lightens up,* ACS Photonics **6**, 802 (2019).

[157] M. Peter, A. Hildebrandt, C. Schlickriede, K. Gharib, T. Zentgraf, J. Förstner, and S. Linden, *Directional Emission from Dielectric Leaky-Wave Nanoantennas,* Nano Letters **17**, 4178 (2017).

[158] A. Vaskin, S. Mashhadi, M. Steinert, K. E. Chong, D. Keene, S. Nanz, A. Abass, E. Rusak, D. Y. Choi, I. Fernandez-Corbaton, T. Pertsch, C. Rockstuhl, M. A. Noginov, Y. S. Kivshar, D. N. Neshev, N. Noginova, and I. Staude, *Manipulation of Magnetic Dipole Emission from Eu 3+ with Mie-Resonant Dielectric Metasurfaces,* Nano Letters **19**, 1015 (2019).

[159] N. E. Watkins, J. Guan, B. T. Diroll, K. R. Williams, R. D. Schaller, and T. W. Odom, *Surface Normal Lasing from CdSe Nanoplatelets Coupled to Aluminum Plasmonic Nanoparticle Lattices,* The Journal of Physical Chemistry C **125**, 19874 (2021).

[160] M. Aellen, A. A. Rossinelli, R. C. Keitel, R. Brechbühler, F. V. Antolinez, S. G. Rodrigo, J. Cui, and D. J. Norris, *Role of Gain in Fabry–Pérot Surface Plasmon Polariton Lasers,* ACS Photonics **9**, 630 (2022).

[161] M. Wu, L. Ding, R. P. Sabatini, L. K. Sagar, G. Bappi, R. Paniagua-Domínguez, E. H. Sargent, and A. I. Kuznetsov, *Bound State in the Continuum in Nanoantenna-Coupled Slab Waveguide Enables Low-Threshold Quantum-Dot Lasing,* Nano Letters **21**, 9754 (2021).

[162] T. Veeken, B. Daiber, H. Agrawal, M. Aarts, E. Alarcón-Lladó, E. C. Garnett, B. Ehrler, J. van de Groep, and A. Polman, *Directional quantum dot emission by soft-stamping on silicon Mie resonators,* Nanoscale Advances **4**, 1088 (2022).

[163] A. A. Rossinelli, H. Rojo, A. S. Mule, M. Aellen, A. Cocina, E. De Leo, R. Schäublin, and D. J. Norris, *Compositional Grading for Efficient and Narrowband Emission in CdSe-Based Core/Shell Nanoplatelets,* Chemistry of Materials **31**, 9567 (2019).

[164] J. van de Groep and A. Polman, *Designing dielectric resonators on substrates: Combining magnetic and electric resonances,* Optics Express **21**, 26285 (2013).

[165] S. Ha, R. Janissen, Y. Y. Ussembayev, M. M. Van Oene, B. Solano, and N. H. Dekker, *Tunable top-down fabrication and functional surface coating of single-crystal titanium dioxide nanostructures and nanoparticles,* Nanoscale **8**, 10739 (2016).

[166] J. Van De Groep, P. Spinelli, and A. Polman, *Single-Step Soft-Imprinted Large-Area Nanopatterned Antireflection Coating,* Nano Letters **15**, 4223 (2015).

[167] V. Liu and S. Fan, *S4 : A free electromagnetic solver for layered periodic structures,* Computer Physics Communications **183**, 2233 (2012).

[168] I. Sersic, C. Tuambilangana, and A. Femius Koenderink, *Fourier microscopy of single plasmonic scatterers,* New Journal of Physics **13**, 083019 (2011).

[169] A. Richter, M. Hermle, and S. W. Glunz, *Reassessment of the limiting efficiency for crystalline silicon solar cells,* IEEE Journal of Photovoltaics **3**, 1184 (2013).

[170] K. Yoshikawa, H. Kawasaki, W. Yoshida, T. Irie, K. Konishi, K. Nakano, T. Uto, D. Adachi, M. Kanematsu, H. Uzu, and K. Yamamoto, *Silicon heterojunction solar cell with interdigitated back contacts for a photoconversion efficiency over 26%,* Nature Energy **2**, 17032 (2017).

[171] J. G. Ingersoll, *Simplified calculation of solar cell temperatures in terrestrial photovoltaic arrays,* Journal of Solar Energy Engineering, Transactions of the ASME **108**, 95 (1986).

[172] O. Dupré, R. Vaillon, and M. A. Green, *Thermal Behavior of Photovoltaic Devices*, 1st ed. (Springer International Publishing, 2017) p. 130.

[173] E. Skoplaki and J. A. Palyvos, *On the temperature dependence of photovoltaic module electrical performance: A review of efficiency/power correlations,* Solar Energy **83**, 614 (2009).

[174] C. R. Osterwald and T. J. McMahon, *History of accelerated and qualification testing of terrestrial photovoltaic modules: A literature review,* Progress in Photovoltaics: Research and Applications **17**, 11 (2009).

[175] D. H. Otth and R. G. Ross, *Assessing Photovoltaic Module Degradation and Lifetime From Long Term Environmental Tests,* in *29th Institute of Environmental Sciences Technical Meeting* (Los Angeles, CA, 1983) pp. 121–126.

[176] M. Kumar and A. Kumar, *Performance assessment and degradation analysis of solar photovoltaic technologies: A review,* Renewable and Sustainable Energy Reviews **78**, 554 (2017).

[177] S. Fan and W. Li, *Photonics and thermodynamics concepts in radiative cooling,* Nature Photonics (2022), 10.1038/s41566-021-00921-9.

[178] D. Beysens, I. Milimouk, V. Nikolayev, M. Muselli, and J. Marcillat, *Using radiative cooling to condense atmospheric vapor: A study to improve water yield,* Journal of Hydrology **276**, 1 (2003).

[179] D. Zhao, X. Yin, J. Xu, G. Tan, and R. Yang, *Radiative sky cooling-assisted thermoelectric cooling system for building applications,* Energy **190**, 116322 (2020).

[180] A. P. Raman, M. A. Anoma, L. Zhu, E. Rephaeli, and S. Fan, *Passive radiative cooling below ambient air temperature under direct sunlight,* Nature **515**, 540 (2014).

[181] W. Li, Y. Shi, K. Chen, L. Zhu, and S. Fan, *A Comprehensive Photonic Approach for Solar Cell Cooling,* ACS Photonics **4**, 774 (2017).

[182] M. Zahir and M. Benlattar, *Design of radiative cooler based on porous TiO 2 for improving solar cells' performance ,* Applied Optics **60**, 445 (2021).

[183] G. Perrakis, A. C. Tasolamprou, G. Kenanakis, E. N. Economou, S. Tzortzakis, and M. Kafesaki, *Combined nano and micro structuring for enhanced radiative cooling and efficiency of photovoltaic cells,* Scientific Reports **11**, 1 (2021).

[184] J. Jaramillo-Fernandez, G. L. Whitworth, J. A. Pariente, A. Blanco, P. D. Garcia, C. Lopez, and C. M. Sotomayor-Torres, *A Self-Assembled 2D Thermofunctional Material for Radiative Cooling,* Small **15**, 1 (2019).

[185] L. Long, Y. Yang, and L. Wang, *Simultaneously enhanced solar absorption and radiative cooling with thin silica micro-grating coatings for silicon solar cells,* Solar Energy Materials and Solar Cells **197**, 19 (2019).

[186] E. Lee and T. Luo, *Black body-like radiative cooling for flexible thin-film solar cells,* Solar Energy Materials and Solar Cells **194**, 222 (2019).

[187] L. Zhu, A. Raman, K. X. Wang, M. A. Anoma, and S. Fan, *Radiative cooling of solar cells,* Optica **1**, 32 (2014).

[188] L. Zhu, A. P. Raman, and S. Fan, *Radiative cooling of solar absorbers using a visibly transparent photonic crystal thermal blackbody,* Proceedings of the National Academy of Sciences **112**, 12282 (2015).

[189] M. Gao, Y. Xia, R. Li, Z. Zhang, Y. He, C. Zhang, L. Chen, L. Qi, Y. Si, Q. Zhang, and Y. Zheng, *The design of near-perfect spectrum-selective mirror based on photonic structures for passive cooling of silicon solar cells,* Nanomaterials **10**, 1 (2020).

[190] B. Zhao, M. Hu, X. Ao, Q. Xuan, and G. Pei, *Comprehensive photonic approach for diurnal photovoltaic and nocturnal radiative cooling,* Solar Energy Materials and Solar Cells **178**, 266 (2018).

[191] Q. Zhai and Q. Zhu, *Radiative cooling film with self-cleaning function,* Solar Energy Materials and Solar Cells **228**, 111117 (2021).

[192] G. Chen, Y. Wang, J. Qiu, J. Cao, Y. Zou, S. Wang, J. Ouyang, D. Jia, and Y. Zhou, *A visibly transparent radiative cooling film with self-cleaning function produced by solution processing,* Journal of Materials Science and Technology **90**, 76 (2021).

[193] C. Ziming, W. Fuqiang, G. Dayang, L. Huaxu, and S. Yong, *Low-cost radiative cooling blade coating with ultrahigh visible light transmittance and emission within an "atmospheric window",* Solar Energy Materials and Solar Cells **213**, 110563 (2020).

[194] R. Kitamura, L. Pilon, and M. Jonasz, *Optical constants of silica glass from extreme ultraviolet to far infrared at near room temperature,* Applied Optics **46**, 8118 (2007).

[195] S. Kruk and Y. Kivshar, *Functional Meta-Optics and Nanophotonics Governed by Mie Resonances,* ACS Photonics **4**, 2638 (2017).

[196] A. F. Koenderink, A. Alù, and A. Polman, *Nanophotonics: Shrinking light-based technology,* Science **348**, 516 (2015).

[197] C. Van Lare, F. Lenzmann, M. A. Verschuuren, and A. Polman, *Dielectric Scattering Patterns for Efficient Light Trapping in Thin-Film Solar Cells,* Nano Letters **15**, 4846 (2015).

[198] R. Alaee, R. Filter, D. Lehr, F. Lederer, and C. Rockstuhl, *A generalized Kerker condition for highly directive nanoantennas,* Optics Letters **40**, 2645 (2015).

[199] W. Liu and Y. S. Kivshar, *Generalized Kerker effects in nanophotonics and meta-optics [Invited],* Optics Express **26**, 13085 (2018).

[200] A. C. Overvig, S. A. Mann, and A. Alù, *Thermal Metasurfaces: Complete Emission Control by Combining Local and Nonlocal Light-Matter Interactions,* Physical Review X **11**, 21050 (2021).

[201] R. Carminati and J.-J. Greffet, *Near-Field Effects in Spatial Coherence of Thermal Sources,* Physical Review Letters **82**, 1660 (1999).

[202] S. Hava and M. Auslender, *Theoretical dependence of infrared absorption in bulk-doped silicon on carrier concentration,* Applied Optics **32**, 1122 (1993).

[203] E. Hecht, *Optics*, 4th ed. (Addison Wesley, 2002).

[204] S. D. Lord, *A New Software Tool for Computing Earth's Atmospheric Transmission of Near- and Far-Infrared Radiation,* NASA Technical Memorandum 103957 (1992).

[205] Gemini Observatory, *Infrared Atmospheric Transmission Spectra,* (2022).

[206] S. J. Byrnes, *Multilayer optical calculations,* (2016), arXiv:1603.02720 .

[207] R. L. Olmon, B. Slovick, T. W. Johnson, D. Shelton, S.-H. Oh, G. D. Boreman, and M. B. Raschke, *Optical dielectric function of gold,* Physical Review B **86**, 235147 (2012).

[208] C. Hecker, S. Hook, M. van der Meijde, W. Bakker, H. van Werff, H. Wilbrink, F. van Ruitenbeek, B. de Smeth, and F. van der Meer, *Thermal infrared spectrometer for earth science remote sensing applications-instrument modifications and measurement procedures,* Sensors **11**, 10981 (2011).

[209] ITRPV, *International technology roadmap for photovoltaic*, 10th ed. (VDMA Photovoltaic Equipment, 2019).

[210] S. A. Pelaez, C. Deline, S. M. MacAlpine, B. Marion, J. S. Stein, and R. K. Kostuk, *Comparison of Bifacial Solar Irradiance Model Predictions With Field Validation,* IEEE Journal of Photovoltaics **9**, 82 (2019).

[211] G. T. Klise and J. S. Stein, *Sandia National Laboratories*, Tech. Rep. December (Sandia National Laboratories (SNL), Albuquerque, NM, and Livermore, CA (United States), 2009).

[212] M. Abbott, K. McIntosh, B. Sudbury, J. Meydbray, T. H. Fung, M. Umair Khan, Y. Zhang, S. Zou, X. Wang, G. Xing, G. Scardera, and D. Payne, *Annual energy yield analysis of solar cell technology,* in *Conference Record of the IEEE Photovoltaic Specialists Conference* (IEEE, 2019) pp. 3046–3050.

[213] M. R. Vogt, T. Gewohn, K. Bothe, C. Schinke, and R. Brendel, *Impact of Using Spectrally Resolved Ground Albedo Data for Performance Simulations of Bifacial Modules,* in *Proc. 35th European Photovoltaic Solar Energy Conference and Exhibition*, 35 (2018) pp. 1011–1016.

[214] C. K. Lo, Y. S. Lim, and F. A. Rahman, *New integrated simulation tool for the optimum design of bifacial solar panel with reflectors on a specific site,* Renewable Energy **81**, 293 (2015).

[215] R. Couderc, M. Amara, and M. Lemiti, *In-Depth Analysis of Heat Generation in Silicon Solar Cells,* IEEE Journal of Photovoltaics **6**, 1123 (2016).

[216] A. Riverola, A. Mellor, D. Alonso Alvarez, L. Ferre Llin, I. Guarracino, C. Markides, D. Paul, D. Chemisana, and N. Ekins-Daukes, *Mid-infrared emissivity of crystalline silicon solar cells,* Solar Energy Materials and Solar Cells **174**, 607 (2018).

[217] M. Steglich, M. Zilk, A. Bingel, C. Patzig, T. Käsebier, F. Schrempel, E.-B. Kley, and A. Tünnermann, *A normal-incidence PtSi photoemissive detector with black silicon light-trapping,* Journal of Applied Physics **114**, 183102 (2013).

[218] M. Steglich, M. Oehme, T. Käsebier, M. Zilk, K. Kostecki, E.-B. Kley, J. Schulze, and A. Tünnermann, *Ge-on-Si photodiode with black silicon boosted responsivity,* Applied Physics Letters **107**, 051103 (2015).

[219] J. Lv, T. Zhang, P. Zhang, Y. Zhao, and S. Li, *Review Application of Nanostructured Black Silicon,* Nanoscale Research Letters **13**, 110 (2018).

[220] M. Steglich, T. Käsebier, M. Zilk, T. Pertsch, E.-B. Kley, and A. Tünnermann, *The structural and optical properties of black silicon by inductively coupled plasma reactive ion etching,* Journal of Applied Physics **116**, 173503 (2014).

[221] S. Ma, S. Liu, Q. Xu, J. Xu, R. Lu, Y. Liu, and Z. Zhong, *A theoretical study on the optical properties of black silicon,* AIP Advances **8**, 035010 (2018).

[222] M. Kroll, T. Käsebier, M. Otto, R. Salzer, R. Wehrspohn, E.-B. Kley, A. Tünnermann, and T. Pertsch, *Optical modeling of needle like silicon surfaces produced by an ICP-RIE process,* in *Proceedings of SPIE, Photonics for Solar Energy Systems III*, Vol. 7725 (2010) p. 772505.

[223] A. J. Bett, J. Eisenlohr, O. Höhn, P. Repo, H. Savin, B. Bläsi, and J. C. Goldschmidt, *Wave optical simulation of the light trapping properties of black silicon surface textures,* Optics Express **24**, A434 (2016).

[224] M. G. Moharam, T. K. Gaylord, E. B. Grann, and D. A. Pommet, *Formulation for stable and efficient implementation of the rigorous coupled-wave analysis of binary gratings,* Journal of the Optical Society of America A **12**, 1068 (1995).

[225] N. Tucher, H. T. Gebrewold, and B. Bläsi, *Field stitching approach for the wave optical modeling of black silicon structures,* Optics Express **26**, A937 (2018).

[226] N. Tucher, J. Eisenlohr, P. Kiefel, O. Höhn, H. Hauser, M. Peters, C. Müller, J. C. Goldschmidt, and B. Bläsi, *3D optical simulation formalism OPTOS for textured silicon solar cells,* Optics Express **23**, A1720 (2015).

[227] Y. Li, Y. Chen, Z. Ouyang, and A. Lennon, *Angular matrix framework for light trapping analysis of solar cells,* Optics Express **23**, A1707 (2015).

[228] J. Eisenlohr, N. Tucher, H. Hauser, M. Graf, J. Benick, B. Bläsi, J. C. Goldschmidt, and M. Hermle, *Efficiency increase of crystalline silicon solar cells with nanoimprinted rear side gratings for enhanced light trapping,* Solar Energy Materials and Solar Cells **155**, 288 (2016).

[229] A. A. Elsayed, Y. M. Sabry, F. Marty, T. Bourouina, and D. Khalil, *Optical modeling of black silicon using an effective medium/multi-layer approach,* Optics Express **26**, 13443 (2018).

[230] S. Chattopadhyay, Y. Huang, Y. Jen, A. Ganguly, K. Chen, and L. Chen, *Anti-reflecting and photonic nanostructures,* Materials Science and Engineering: R: Reports **69**, 1 (2010).

[231] T. Rahman and S. A. Boden, *Optical Modeling of Black Silicon for Solar Cells Using Effective Index Techniques,* IEEE Journal of Photovoltaics **7**, 1556 (2017).

[232] M. Otto, M. Algasinger, H. Branz, B. Gesemann, T. Gimpel, K. Füchsel, T. Käsebier, S. Kontermann, S. Koynov, X. Li, V. Naumann, J. Oh, A. N. Sprafke, J. Ziegler, M. Zilk, and R. B. Wehrspohn, *Black Silicon Photovoltaics,* Advanced Optical Materials **3**, 147 (2015).

[233] K. Tang, R. A. Dimenna, and R. O. Buckius, *Regions of validity of the geometric optics approximation for angular scattering from very rough surfaces,* International Journal of Heat and Mass Transfer **40**, 49 (1996).

[234] M. M. Plakhotnyuk, M. Gaudig, R. S. Davidsen, J. M. Lindhard, J. Hirsch, D. Lausch, M. S. Schmidt, E. Stamate, and O. Hansen, *Low surface damage dry etched black silicon,* Journal of Applied Physics **122**, 143101 (2017).

[235] P. Repo, J. Benick, G. von Gastrow, V. Vähänissi, F. D. Heinz, J. Schön, M. C. Schubert, and H. Savin, *Passivation of black silicon boron emitters with atomic layer deposited aluminum oxide,* Physica Status Solidi - Rapid Research Letters **7**, 950 (2013).

[236] B. Bhushan, *Surface roughness analysis and measurement techniques,* in *Modern Tribology Handbook*, edited by T. Inc and Francis (CRC Press, 2000) Chap. 2.2.2.4, p. 1760.

[237] D. Bergstrom, *Computer program: Rough surface generation and analysis,* (2012).

[238] D. Nečas and P. Klapetek, *Gwyddion: an open-source software for SPM data analysis,* Open Physics **10**, 181 (2012).

[239] D. Payne, M. Abbott, A. L. Claville, Y. Zeng, T. H. Fung, K. McIntosh, J. C. Campa, R. Davidson, M. Plakhotnyuk, and D. Bagnall, *Rapid optical modelling of plasma textured silicon,* in *Proceedings of the IEEE EUPVSEC 2017*, 33 (2017) pp. 897–901.

[240] M. Khardani, M. Bouaïcha, and B. Bessaïs, *Bruggeman effective medium approach for modelling optical properties of porous silicon: Comparison with experiment,* Physica Status Solidi (C) Current Topics in Solid State Physics **4**, 1986 (2007).

[241] B. C. Bergner, T. A. Germer, and T. J. Suleski, *Effective medium approximations for modeling optical reflectance from gratings with rough edges,* Journal of the Optical Society of America A **27**, 1083 (2010).

[242] Y. Battie, A. En Naciri, W. Chamorro, and D. Horwat, *Generalized Effective Medium Theory to Extract the Optical Properties of Two-Dimensional Nonspherical Metallic Nanoparticle Layers,* The Journal of Physical Chemistry C **118**, 4899 (2014).

[243] O. Zhuromskyy, *Applicability of Effective Medium Approximations to Modelling of Mesocrystal Optical Properties,* Crystals **7**, 1 (2016).

[244] J. Maxwell Garnett, *XII. Colours in metal glasses and in metallic films,* Philosophical Transactions of the Royal Society A **203**, 385 (1904).

[245] V. A. Markel, *Introduction to the Maxwell Garnett approximation: tutorial,* Journal of the Optical Society of America A **33**, 1244 (2016).

[246] J. Humlicek, *Ellipsometry at the Nanoscale*, edited by M. Losurdo and K. Hingerl (Springer Berlin Heidelberg, Berlin, Heidelberg, 2013) pp. 145–178.

[247] ANSYS Lumerical, *FDTD Solutions,* (2018).

[248] P. Spinelli, M. A. Verschuuren, and A. Polman, *Broadband omnidirectional antireflection coating based on subwavelength surface Mie resonators,* Nature Communications **3**, 1 (2012).

[249] J. Zhu, Z. Yu, G. F. Burkhart, C. M. Hsu, S. T. Connor, Y. Xu, Q. Wang, M. McGehee, S. Fan, and Y. Cui, *Optical absorption enhancement in amorphous silicon nanowire and nanocone arrays,* Nano Letters **9**, 279 (2009).

[250] S. Jeong, M. D. McGehee, and Y. Cui, *All-back-contact ultra-thin silicon nanocone solar cells with 13.7% power conversion efficiency,* Nature Communications **4**, 2950 (2013).

[251] E. F. Pecora, A. Cordaro, P. G. Kik, and M. L. Brongersma, *Broadband Antireflection Coatings Employing Multiresonant Dielectric Metasurfaces,* ACS Photonics **5**, 4456 (2018).

[252] Y. Wang, N. Lu, H. Xu, G. Shi, M. Xu, X. Lin, H. Li, W. Wang, D. Qi, Y. Lu, and L. Chi, *Biomimetic corrugated silicon nanocone arrays for self-cleaning antireflection coatings,* Nano Research **3**, 520 (2010).

[253] M. M. Hossain and M. Gu, *Radiative Cooling: Principles, Progress, and Potentials,* Advanced Science **3**, 1500360 (2016).

[254] P. Repo, A. Haarahiltunen, L. Sainiemi, M. Yli-Koski, H. Talvitie, M. C. Schubert, and H. Savin, *Effective Passivation of Black Silicon Surfaces by Atomic Layer Deposition,* IEEE Journal of Photovoltaics **3**, 90 (2013).

[255] A. Ingenito, O. Isabella, and M. Zeman, *Nano-cones on micro-pyramids: modulated surface textures for maximal spectral response and high-efficiency solar cells,* Progress in Photovoltaics: Research and Applications **23**, 1649 (2015).

[256] X. Liu, P. R. Coxon, M. Peters, B. Hoex, J. M. Cole, and D. J. Fray, *Black silicon: fabrication methods, properties and solar energy applications,* Energy Environ. Sci. **7**, 3223 (2014).

[257] Y. Xia, B. Liu, J. Liu, Z. Shen, and C. Li, *A novel method to produce black silicon for solar cells,* Solar Energy **85**, 1574 (2011).

[258] R. Bilyalov, R. Lüdemann, W. Wettling, L. Stalmans, J. Poortmans, J. Nijs, L. Schirone, G. Sotgiu, S. Strehlke, and C. Lévy-Clément, *Multicrystalline silicon solar cells with porous silicon emitter,* Solar Energy Materials and Solar Cells **60**, 391 (2000).

[259] M. B. Rabha, W. Dimassi, M. Bouaïcha, H. Ezzaouia, and B. Bessais, *Laser-beam-induced current mapping evaluation of porous silicon-based passivation in polycrystalline silicon solar cells,* Solar Energy **83**, 721 (2009).

[260] T. Pasanen, V. Vähänissi, N. Theut, and H. Savin, *Surface passivation of black silicon phosphorus emitters with atomic layer deposited SiO2/Al2O3 stacks,* Energy Procedia **124**, 307 (2017).

[261] J. Wu, H. Wu, X. Chen, Z. Yao, D. Zhang, S. Su, M. Zhang, F. Jiang, and G. Xing, *21.4% efficiency bifacial multi-Si PERC cells and 410W modules,* in *2019 IEEE 46th Photovoltaic Specialists Conference (PVSC)*, 199 (IEEE, 2019) pp. 1466–1470.

[262] M. U. Khan, G. Scardera, S. Zou, D. Zhang, and M. Abbott, *The Role of Metal-Catalyzed Chemical Etching Black Silicon in the Reduction of Light- and Elevated Temperature-Induced Degradation in P-Type Multicrystalline Wafers,* IEEE Journal of Photovoltaics **11**, 627 (2021).

[263] F. Shimura, *Semiconductor silicon crystal technology*, 1st ed., Vol. 26 (Academic Press, 1989).

[264] I. Synopsys, *Sentaurus Device - An advanced multidimensional (1D/2D/3D) device simulator,* (2021).

[265] PV-Lighthouse, *SunSolve™,* (2019).

[266] K. Füchsel, M. Kroll, M. Otto, M. Steglich, A. Bingel, T. Käsebier, R. B. Wehrspohn, E.-B. Kley, T. Pertsch, and A. Tünnermann, *Black Silicon Photovoltaics,* in *Photon Management in Solar Cells*, Vol. 3 (Wiley-VCH Verlag GmbH & Co. KGaA, Weinheim, Germany, 2015) pp. 117–151.

[267] Y. Zhang, C. Kong, R. S. Davidsen, G. Scardera, L. Duan, K. T. Khoo, D. N. Payne, B. Hoex, and M. Abbott, *3D characterisation using plasma FIB-SEM: A large-area tomography technique for complex surfaces like black silicon,* Ultramicroscopy **218**, 113084 (2020).

[268] F. J. Giessibl, *Advances in atomic force microscopy,* Reviews of Modern Physics **75**, 949 (2003).

[269] N. Jalili and K. Laxminarayana, *A review of atomic force microscopy imaging systems: application to molecular metrology and biological sciences,* Mechatronics **14**, 907 (2004).

[270] D. Sarid, *Review of scanning force microscopy,* Journal of Vacuum Science & Technology B: Microelectronics and Nanometer Structures **9**, 431 (1991).

[271] E. Ukraintsev, A. Kromka, H. Kozak, Z. Reme, and B. Rezek, *Artifacts in Atomic Force Microscopy of Biological Samples,* in *Atomic Force Microscopy Investigations into Biology - From Cell to Protein* (InTech, 2012).

[272] J. I. Paredes, A. Martinez-Alonso, and J. M. D. Tascon, *Adhesion artefacts in atomic force microscopy imaging,* Journal of Microscopy **200**, 109 (2000).

[273] U. D. Schwarz, H. Haefke, P. Reimann, and H.-J. Güntherodt, *Tip artefacts in scanning force microscopy,* Journal of Microscopy **173**, 183 (1994).

[274] T. H. Fung, T. Veeken, D. Payne, B. Veettil, A. Polman, and M. Abbott, *Application and validity of the effective medium approximation to the optical properties of nano-textured silicon coated with a dielectric layer,* Optics Express **27**, 38645 (2019).

[275] T. H. Fung, M. U. Khan, Y. Zhang, N. J. Western, D. N. R. Payne, K. R. Mclntosh, and M. D. Abbott, *Improved Ray Tracing on Random Pyramid Texture via Application of Phong Scattering,* IEEE Journal of Photovoltaics **9**, 591 (2019).

[276] Y. Ge, F. Zhao, L. Wang, and X. Wang, *A novel perspective on the design of thermochromic VO2 films: Combining ab initio calculations with FDTD simulations,* Surface and Coatings Technology **402**, 126493 (2020).

[277] D. Payne, T. H. Fung, M. U. Khan, J. Cruz-Campa, K. McIntosh, and M. Abbott, *Understanding the optics of industrial black silicon,* in *AIP Conference Proceedings*, Vol. 1999 (2018) p. 050007.

[278] G. Scardera, S. Wang, Y. Zhang, M. U. Khan, S. Zou, D. Zhang, R. S. Davidsen, O. Hansen, L. Mai, D. N. R. Payne, B. Hoex, and M. D. Abbott, *On the Enhanced Phosphorus Doping of Nanotextured Black Silicon,* IEEE Journal of Photovoltaics **11**, 298 (2021).

[279] A. Fell, K. C. Fong, K. R. McIntosh, E. Franklin, and A. W. Blakers, *3-D Simulation of Interdigitated-Back-Contact Silicon Solar Cells With Quokka Including Perimeter Losses,* IEEE Journal of Photovoltaics **4**, 1040 (2014).

[280] Y. Zhang, D. N. R. Payne, C. Kong, M. U. Khan, T. H. Fung, R. S. Davidsen, O. Hansen, G. Scardera, M. D. Abbott, and B. Hoex, *Advanced Characterisation of Black Silicon Surface Topography with 3D PFIB-SEM,* in *2019 IEEE 46th Photovoltaic Specialists Conference (PVSC)* (IEEE, Chicago, 2019) pp. 0825–0828.

[281] Y. Zhang, C. Kong, G. Scardera, M. Abbott, D. N. Payne, and B. Hoex, *Large volume tomography using plasma FIB-SEM: A comprehensive case study on black silicon,* Ultramicroscopy **233**, 113458 (2022).

[282] H. R. Philipp and E. A. Taft, *Optical Constants of Silicon in the Region 1 to 10 eV,* Physical Review **120**, 37 (1960).

[283] M. A. Green, *Self-consistent optical parameters of intrinsic silicon at 300K including temperature coefficients,* Solar Energy Materials and Solar Cells **92**, 1305 (2008).

[284] M. Welkowsky and R. Braunstein, *Interband Transitions and Exciton Effects in Semiconductors,* Physical Review B **5**, 497 (1972).

[285] G. Jellison, *Optical functions of GaAs, GaP, and Ge determined by two-channel polarization modulation ellipsometry,* Optical Materials **1**, 151 (1992).

[286] W. Theiß, *Optical properties of porous silicon,* Surface Science Reports **29**, 91 (1997).

[287] G. Scardera, D. Payne, M. Khan, Y. Zhang, A. Soeriyadi, S. Zou, D. Zhang, R. Davidsen, O. Hansen, B. Hoex, and M. Abbott, *Silicon Nanotexture Surface Area Mapping Using Ultraviolet Reflectance,* IEEE Journal of Photovoltaics **11**, 1291 (2021).

[288] H.-C. Yuan, V. E. Yost, M. R. Page, P. Stradins, D. L. Meier, and H. M. Branz, *Efficient black silicon solar cell with a density-graded nanoporous surface: Optical properties, performance limitations, and design rules,* Applied Physics Letters **95**, 123501 (2009).

[289] H. M. Branz, V. E. Yost, S. Ward, K. M. Jones, B. To, and P. Stradins, *Nanostructured black silicon and the optical reflectance of graded-density surfaces,* Applied Physics Letters **94**, 231121 (2009).

[290] F. Patolsky, G. Zheng, and C. M. Lieber, *Nanowire sensors for medicine and the life sciences,* Nanomedicine **1**, 51 (2006).

[291] F. Patolsky, B. P. Timko, G. Zheng, and C. M. Lieber, *Nanowire-Based Nanoelectronic Devices in the Life Sciences,* MRS Bulletin **32**, 142 (2007).

[292] M. J. Schmand, D. Henseler, R. Grazioso, N. Zhang, and M. S. Andreaco, *Patent: Medical Imaging with Black Silicon Photodetector,* (2010).

[293] M. U. Pralle, J. E. Carey, H. Homayoon, S. Alie, J. Sickler, X. Li, J. Jiang, D. Miller, C. Palsule, and J. McKee, *Black silicon enhanced photodetectors: a path to IR CMOS,* in *Infrared Technology and Applications XXXVI*, Vol. 7660, edited by B. F. Andresen, G. F. Fulop, and P. R. Norton (2010) p. 76600N.

[294] G. Seniutinas, G. Gervinskas, R. Verma, B. D. Gupta, F. Lapierre, P. R. Stoddart, F. Clark, S. L. McArthur, and S. Juodkazis, *Versatile SERS sensing based on black silicon,* Optics Express **23**, 6763 (2015).

[295] A. P. Goodey, S. M. Eichfeld, K.-k. Lew, J. M. Redwing, and T. E. Mallouk, *Silicon Nanowire Array Photoelectrochemical Cells,* Journal of the American Chemical Society **129**, 12344 (2007).

[296] J. R. Szczech and S. Jin, *Nanostructured silicon for high capacity lithium battery anodes,* Energy Environ. Sci. **4**, 56 (2011).

[297] J. Oh, T. G. Deutsch, H.-C. Yuan, and H. M. Branz, *Nanoporous black silicon photocathode for H2 production by photoelectrochemical water splitting,* Energy & Environmental Science **4**, 1690 (2011).

[298] I. Oh, J. Kye, and S. Hwang, *Enhanced Photoelectrochemical Hydrogen Production from Silicon Nanowire Array Photocathode,* Nano Letters **12**, 298 (2012).

[299] R. Carter, S. Chatterjee, E. Gordon, K. Share, W. R. Erwin, A. P. Cohn, R. Bardhan, and C. L. Pint, *Corrosion resistant three-dimensional nanotextured silicon for water photo-oxidation,* Nanoscale **7**, 16755 (2015).

[300] Y. Yu, Z. Zhang, X. Yin, A. Kvit, Q. Liao, Z. Kang, X. Yan, Y. Zhang, and X. Wang, *Enhanced photoelectrochemical efficiency and stability using a conformal TiO2 film on a black silicon photoanode,* Nature Energy **2**, 17045 (2017).

[301] Y.-L. Deng and Y.-J. Juang, *Black silicon SERS substrate: Effect of surface morphology on SERS detection and application of single algal cell analysis,* Biosensors and Bioelectronics **53**, 37 (2014).

[302] E. P. Ivanova, J. Hasan, H. K. Webb, G. Gervinskas, S. Juodkazis, V. K. Truong, A. H. Wu, R. N. Lamb, V. A. Baulin, G. S. Watson, J. A. Watson, D. E. Mainwaring, and R. J. Crawford, *Bactericidal activity of black silicon,* Nature Communications **4**, 2838 (2013).